FABRICATION AND CHARACTERIZATION OF GAN VISIBLE-BLIND ULTRAVIOLET AVALANCHE PHOTODIODES

A Thesis
Presented to
The Academic Faculty

by

Yun Zhang

In Partial Fulfillment
of the Requirements for the Degree
Master of Science in the
School of Electrical and Computer Engineering

Georgia Institute of Technology

August, 2009

FABRICATION AND CHARACTERIZATION OF GAN VISIBLE-BLIND ULTRAVIOLET AVALANCHE PHOTODIODES

Approved by:

Dr. Shyh-Chiang Shen, Advisor
School of Electrical and Computer Engineering
Georgia Institute of Technology

Dr. Russell D. Dupuis
School of Electrical and Computer Engineering
Georgia Institute of Technology

Dr. William A. Doolittle
School of Electrical and Computer Engineering
Georgia Institute of Technology

Date Approved: May 15, 2009

ACKNOWLEDGEMENTS

I would like to express my sincere gratitude to all those who provide me with the opportunity to complete this thesis. First, I would like to thank my advisor, Professor Shyh-Chiang Shen, for leading me into this fantastic world of III-nitride electronics, for providing me the intelligence and inspiration during my research, and for teaching me to take my own responsibility. I would like to thank Professors Russell D. Dupuis and Alan Doolittle for kindly serving on my reading committee.

I would like to thank my colleagues in the SRL group: Kevin Brenner, Bravishma Narayan, Yi-Che Lee, Zen Mehra, Mike Evans, Ofer Finkler, Matt Britt, and Mike Brainin. I would especially like to express my thanks to Dr. Dongwon Yoo, Dr. Hee-Jin Kim, Dr. Jianping Liu, Dr. Jae-Hyun Ryou and Suk Choi in the Center of Compound Semiconductor at Georgia Tech for providing me with high-qualify materials, to Dr. Jae-Boum Limb for his help with my fabrication. I would also like to acknowledge the help from Dr. Xiaogang Bai in Professor Joe C. Campbell's group at the University of Virginia for the Geiger-mode operation testing.

Finally, but most important, I want to deliver my deepest appreciation to my parents for their endless support through every accomplishment of my life.

TABLE OF CONTENTS

LIST OF TABLES

LIST OF FIGURES

SUMMARY

This thesis describes the fabrication and characterization of GaN homojunction visible-blind ultraviolet (UV) *p-i-n* avalanche photodiodes (APDs) grown by metalorganic chemical vapor deposition (MOCVD) on free-standing bulk GaN substrates. The objective of this research is to develop GaN UV *p-i-n* APDs with high linear-mode avalanche gains and the Geiger-mode operation for single photon detection. Low noise, high responsivity, and high detectivity are also required for fabricated APDs used as photodiodes in the photovoltaic mode (zero bias) and the photoconductive mode (low reverse bias).

High material defect density and immature fabrication technology have hampered the development of III-nitride APDs in the past. In this thesis, sidewall leakage reduction methods have been developed to achieve significant improvement in dark current density, noise performance, and photo detection performance. A record linear-mode avalanche gain > 10^5 for GaN APDs was demonstrated at λ = 360 nm. The first Geiger-mode deep UV (DUV) APD using front-illuminated homojunction *p-i-n* diode structure on a free-standing bulk GaN substrate was also measured with single photo detection efficiency (SPDE) of 1.0 % and dark count probability (DCP) of 0.03 at 265 nm.

The performance of fabricated homojunction GaN *p-i-n* photodiodes was also evaluated in the photoconductive mode as well as the photovoltaic mode. For an 80-μm-diameter device biased at – 20 V (in the photoconductive mode) the dark current density is lower than 40 pA/cm^2 which is the lowest value achieved for any III-nitride photodiode so far. Its responsivity is 0.140

A/W at 360 nm with an ultraviolet-visible rejection ratio of 8×10^{3}. The room-temperature noise equivalent power is 4.27×10^{-17} W-Hz$^{-0.5}$ and the detectivity D* is 1.66×10^{14} cm-Hz$^{0.5}$-W^{-1} at – 20 V. The minimum detectable optical power is as low as 100 fW. They are among the best values reported for reverse-biased GaN *p-i-n* photodiodes to date.

CHAPTER 1 INTRODUCTION

1.1 Group III-nitride semiconductor structure and characteristics

With Gallium (Ga), Aluminum (Al) and Indium (In) from column III of the periodic table of elements, nitrogen (N) can form III-nitride compound semiconductors, such as gallium nitride (GaN), aluminum nitride (AlN), indium nitride (InN), and their ternary and quaternary alloys. Although the zinc blende and rock salt phases exist, the major crystal structure of III-nitride semiconductors at low pressure (e.g. atmosphere pressure) is the wurtzite phase. As shown in **Figure 1.1**, the wurtzite structure for III-nitride materials has a hexagonal unit cell with *a* and *c* as the lattice constants. Major material properties of binary III-nitride compound semiconductors as well as some other important semiconductors are listed in **Table 1.1**.

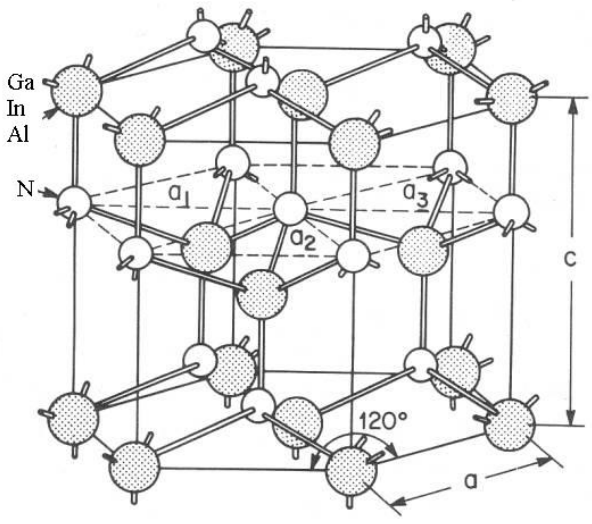

Figure 1.1. Diagram of the wurtzite structure the binary III-nitride materials [1].

Table 1.1. The major material properties of binary III-nitride compound semiconductors and some other important semiconductors (at 300 K) [2-9].

Material Properties	GaN	AlN	InN	Si	Ge	GaAs	InP	4H-SiC
Structure	W	W	W	D	D	Z	Z	W
Lattice Const. (Å)	a=3.189 c=5.182	a=3.111 c=4.978	a=3.544 c=5.718	5.431	5.646	5.653	5.869	a=3.073 c=10.05
Bandgap (eV)	3.44	6.2	0.7 ~ 1.0	1.12	0.66	1.42	1.35	3.26
Nature of Bandgap	D	D	D	I	I	D	D	I
Breakdown Field (MV/cm)	5	1.2 ~ 1.8	--	0.25 ~ 0.8	0.1	0.3 ~ 0.9	0.5	3 ~ 5
Electron Saturated Velocity (10^7 cm/s)	2.5	1.9	3.4	2.3	3.1	0.7	3.9	1.9
Electron Mobility (cm^2/Vs)	1000	300	3200	1400	3900	8000	5400	900
Hole Mobility (cm^2/Vs)	400	14	--	500	1900	400	200	120
Thermal Conductivity ($W/cm^{-1}K^{-1}$)	2.0 ~ 2.4	3.0 ~ 3.3	0.6 ~ 1.0	1.56	0.58	0.46	0.68	3.7
Dielectric Constant (static)	10.4	8.5	15.3	11.7	16.0	12.9	12.6	9.66
Refractive index	2.3	2.1 ~ 2.2	2.9 ~ 3.05	3.42	4.0	3.3	3.1	2.55

Note: W = wurtzite, D = diamond, Z = Zincblende. D, I = direct, indirect bandgap

III-nitride with a wurtzite structure is a direct bandgap semiconductor. As shown in Figure 1.2, By tuning the composition of column III elements (lattice-mismatch issue needs to be considered in the material growth) the bandgap energy of III-nitride materials can cover the region from 0.7 eV (InN) to 6.2 eV (AlN) with the corresponding spectral region from the

infrared (1.77 μm) to the deep ultraviolet (DUV) (200 nm). The direct and tunable bandgap property makes the III-nitride materials excellent choices for optoelectronic devices including visible and UV light emitting diodes (LEDs), laser diodes (LDs), UV photodiodes and avalanche photodiodes (APDs). Furthermore, different from conventional semiconductors, such as silicon (Si), Germanium (Ge), Indium phosphide (InP) and gallium arsenide (GaAs), wide-bandgap III-nitride materials own the advantages of higher breakdown filed, higher thermal conductivity, and better chemical and material stability, indicating that they are more suitable for high power, high voltage devices working in harsh environment. With the development of the material growth technology, the carrier mobility in III-nitride materials is much higher than before, which is very important for high speed devices.

In this thesis, the focus will be placed on the fabrication and characterization of GaN-based (Eg=3.44 eV, λ=360 nm) visible-blind UV *p-i-n* APDs.

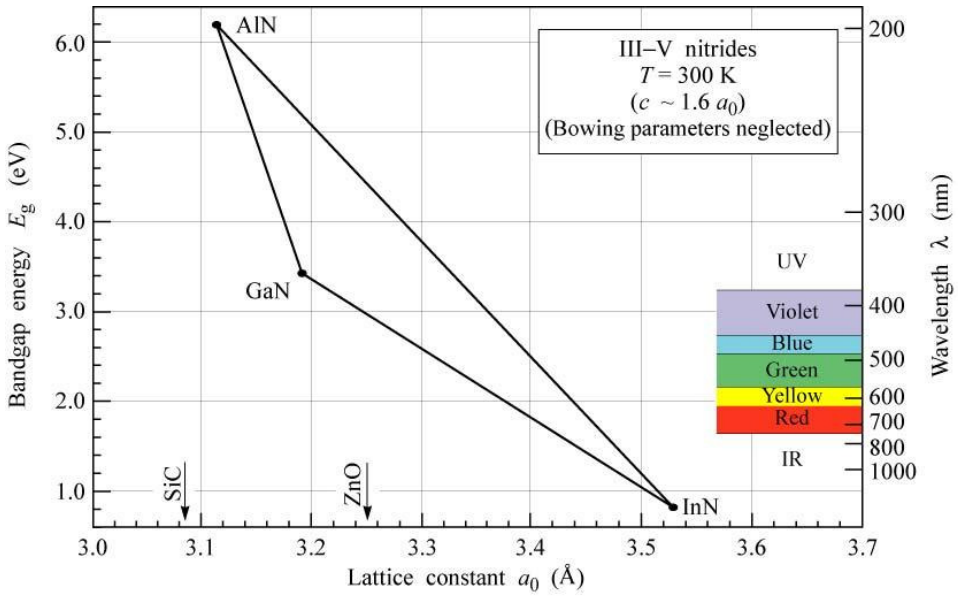

Figure 1.2. Bandgap energy versus lattice constant of III-nitride semiconductors at room temperature [10].

1.2 Motivation for III-nitride avalanche photodiodes

Ultraviolet (UV) light is usually defined as electromagnetic radiation with a wavelength between violet and x-rays, in the range of 10 nm to 400 nm. There are three major spectral bands in the UV region: UVA (400 nm to 320 nm), UVB (320 nm to 280 nm), and UVC (280 nm to 100 nm) [11]. UV detectors with spectral response shorter than 400 nm cannot collect signals from visible radiation, so they are named visible-blind UV detectors. On the same way, the solar-blind UV detectors can also be defined as follows. The Sun, as the biggest natural UV source, emits UV radiation in all of UVA, UVB, and UVC regions. The UVC energy is usually considered to be zero on the earth's surface because of the high absorption from the ozone layer and gases in the atmosphere. UV detectors that are only sensitive to the UVC energy are therefore called solar-blind.

Highly sensitive UV photodetectors are of great importance in numerous scientific, civilian and military applications such as biological agent detection [12], UV astronomy [13], flame detection [14], covert communications [15] and missile tracing. In these cases, high internal gain, low dark current, and sometimes single photon detection are desired because the signal level is extremely low. Photomultiplier tubes (PMTs) are widely used for these low-level UV detections as a common solution because they provide optical gains on the order of one million with low dark current. However, PMTs have the disadvantages of a low quantum efficiency of the photocathode for UV light, high operation voltages (> 1000 V), and the cooling system requirement for the photocathode [16]. The need of expensive filters for visible-blind or solar-blind detection and the large and fragile body are also seriously restricting their applications in harsh environment and room-limited conditions. To find a possible replacement,

lots of research has been done for the development of high-quality semiconductor avalanche photodiodes (APDs) that can provide a large optical gain combined with the benefits of small size, high reliability, high speed, low operation voltage, low power consumption, and the possibility of the Geiger-mode operation (to achieve single photon detection) and all-solid-state integration. At present, UV-enhanced Si APDs are the most commonly used commercial semiconductor detectors for the weak UV detection. The mature and standardized Si technology makes the Si APD a cheap (compared to a PMT system) and robust product. However, the relatively narrow bandgap energy (1.12 eV), high dark current and broad spectral response are major issues for Si APDs. The typical dark current density of a commercial UV-enhanced Si APD (Hamamatsu® S9073) is 0.64 $\mu A/cm^2$ at a gain of 50 and the spectral response is from 200 nm to 1000 nm with a peak at 620 nm (orange-red light) [17]. They cannot provide the noise equivalent power (NEP) requirement of many sensitive UV detections, and they cannot be "blind" to visible or solar light without an external filtering.

From the aspect of semiconductor bandgap theory, the wide-bandgap semiconductors make it possible to realize a filter-free highly sensitive UV detection with lower noise [4] when compared to PMTs or narrow-bandgap-material-based detectors. With the great progress in the wide-bandgap material growth technology since 1990's, the materials such as SiC and III-nitride have been promising candidates for the reliable UV detectors. Wide-bandgap energies of SiC (3.26 eV for 4H-SiC) and III-nitride (3.44 eV for GaN) provide the potential to create photodiodes with low dark current, low noise, and filter-free solar-blind (or visible-blind) spectral response. The wide-bandgap APDs can offer a high internal gain by avalanche

multiplication to improve the detection sensitivity in the UV spectral region, especially by using the Geiger-mode operation in which the single photon detection can be achieved.

4H-SiC-based APDs are widely studied and show good performance for the low noise high optical gain UV detections owing to the material maturity, stability, and the low excess noise factor [18]. The readily available high-quality substrates also result in low material dislocation densities during epitaxy. In fabrication, SiC devices can be passivated with thermal oxide that is grown in a wet oxidation furnace at more than 1000° C. It is a high-quality passivation layer to the etched mesa surface to reduce the sidewall leakage [19]. Prof. Campbell's group at the University of Virginia is leading the SiC APDs research area. In 2007 they demonstrated a linear gain as high as 10^5 (close to PMTs) as well as the Geiger-mode operation at 265 nm [20, 21]. However, SiC photodiodes' responsivity is relatively lower (93 mA/W @ -20 V [20]) than III-nitride photodiodes (usually more than 120 mA/W @ 0 V [22-24]) due to the material's indirect bandgap. For the same reason, the spectral cut-off edge is broadened from the peak to wavelengths longer than 380 nm [25]. It makes the solar-blind detection impossible without filters.

On the other hand, because of the direct and tunable bandgap, the III-nitride materials have gained great interest for optoelectronic devices in both light detection and emission applications. For III-nitride photodiodes, the spectral response peaks very close to the intrinsic absorption wavelength with a sharp cut-off edge, showing a high UV-visible (or UV-solar) rejection ratio. The filter-free visible-blind (or solar-blind) detection can be intrinsically realized. In addition, the III-nitride-based devices are suitable for the hostile-environment applications due to materials' chemical and thermal stability. So III-nitride APDs and photodiodes are considered

more suitable than other semiconductors for UV detections and have been studies extensively in the recent years. Major progresses of III-nitride APDs and photodiodes published in the recent years (2006 ~ 2008) are listed in Table 1.2.

Table 1.2. The major progresses of III-nitride APDs and photodiodes published in 2006 ~2008.

Group	*Material/substrate*	*Type*	*Device area (μm^2)*	*D^*[1] ($cmHz^{0.5}W^{-1}$)*	*I_d[2] (A/cm^2)*	*R_λ[3] (A/W)*	*UVR[4]*	*M[5]*	*SPDE(%)[6]& DCP[7]*
Gatech [26]	GaN/ GaN	PIN	707	--	7n @ -5 V	--	--	1000	--
NCU [27]	GaN/ sapphire	PIN	--	1.7 x 10^{13}	--	0.11 @ 365 nm, 0 V	1200	--	--
NWU [28, 29]	GaN/ sapphire	Back-PIN[8]	Various 225 ~ 14063	--	--	0.082 @ 361 nm, 0 V	--	5700	20% --
Gatech [30]	GaN/ GaN	PIN	4536	--	15n @ -20 V	--	--	10000	--
Gatech [31]	$Al_{0.05}$ GaN/ GaN	PIN	707	--	141n @ -20 V	--	--	50	--
Gatech [32]	GaN/ GaN	PIN	4536	--	100n @ -45 V	--	--	30000	--
Bilkent [22]	GaN/ sapphire	PIN	31416	--	64n @ -5 V	0.23 @ 356 nm, -5 V	6700	--	--
NWU [33]	GaN/ sapphire	Back-SAM[9]	625	--	3.84μ @ -40 V	0.094 @ 360 nm, ~ -70 V	--	51000	--

[1] Effective detectivity
[2] Reverse-biased dark current density
[3] The peak value of responsivity
[4] Ultraviolet-visible rejection ratio
[5] Linear-mode avalanche gain
[6] Single photon detection efficiency
[7] Dark count possibility
[8] Back-illuminated *p-i-n* photodiode
[9] Back-illuminated separate absorption and multiplication photodiode

Table 1.2 (continued). The major progresses of III-nitride APDs and photodiodes published in 2006 ~ 2008.

Group	*Material/substrate*	*Type*	*Device area (μm^2)*	*D* ($cmHz^{0.5}W^{-1}$)*	*I_d (A/cm^2)*	*R_λ (A/W)*	*UVR*	*M*	*SPD E(%) & DCP*
NWU [34]	GaN/ sapphire	Back-PIN	Various 225 ~ 2025	--	--	0.163 @ 352 nm, -20 V	--	5000	--
NWU [35]	GaN/ sapphire	Back-SAM	225	--	8.89µ @ -40 V	0.102 @ 364 nm, -40 V	--	41200	--
CAS [36]	GaN/ sapphire	PIN	31416	--	159n @ -20 V	--	--	57	--
Gatech [37]	GaN/ GaN	PIN	7854	--	5n @ -10V	0.14 @ 360 nm, 0 V	--	10^5	1 % & 0.03
NCKU [23, 38]	GaN/sapphire	MSM	--	2.67 x 10^{10}	--	0.017 @ -0.5 V	14400	--	--
LU [39]	GaN/sapphire	MIS	17671	--	0.33n @ -5 V	0.018 @ 350 nm -3 V	2500	--	--
NCKU [23]	GaN/sapphire	MSM	11400	--	2.5m @ -10 V	0.132 @ 350 nm, -5V	--	--	--
Auburn [40]	GaN/ GaN	Schottky	--	--	--	0.09 @ 360 nm 0V	2 x 10^6	--	--
Bilkent [24]	$Al_{0.4}GaN$/sapphire	Schottky	1257	1.4 x 10^{14}	1µ @ -20 V	0.13 @ 272 nm, -20V	--	1560	--
NIT [41]	AlInN/ sapphire	Schottky	17671	--	12µ @ -5 V	0.14 @ 230 nm 0 V	--	--	--
STU [42]	GaN/sapphire	Shcottky	196350	--	51n @ -3 V	0.015 @ 360 nm 0 V	4 x 10^5	--	--

As shown in Table 1.2, recently high-quality III-nitride-based APDs and photodiodes have been widely reported, including *p-n* junction photodiodes and Schottky-barrier photodiodes. Photodiodes based on the Schottky-barrier junction, such as metal-semiconductor-metal (MSM) photodiodes and Schottky-barrier (metal-semiconductor) photodiodes, have the advantages of high response speeds [4] and the simple fabrication processes that are compatible with field-effect transistor (FET) technology. However, the typical dark current density of the state-of-the-art MSM photodiodes is still three orders higher than that of the *p-n* junction photodiodes due to the fundamental device limitation [4]. It is important to achieve a high Schottky barrier height at the metal-semiconductor interface for smaller leakage current and higher breakdown voltages. Most of the recent papers are focused on the metal-semiconductor interface studies, such as un-activated Mg-doped GaN layers [38, 39] and dielectric/GaN heterojunctions [42]. Although the dark current density can be significantly reduced, the responsivity is degraded at the same time by almost 10 times. Schottky-barrier-based photodiodes are popular for general purpose detections because of the low cost, but they are not suitable for highly sensitive UV detections.

p-n junction photodiodes have the advantages of lower dark current [26], higher responsivity [22], higher detectivity [43, 44], and higher internal gains [32, 33, 35]. To date, the reported III-nitride *p-n* junction photodiodes mainly include *p-i-n* photodiodes [22], *p-i-n* APDs in the linear-mode [30-32, 37, 45] and the Geiger-mode [37, 46], back-illuminated *p-i-n* APDs in the linear-mode [28, 29, 34] and the Geiger-mode [28, 29], and back-illuminated separated absorption and multiplication (SAM) APDs in the linear-mode [33, 35].

APDs are usually much smaller than low-biased photodiodes because of more dislocations on larger sizes. Dislocations seriously increase the dark current and degrade the

multiplication gain, and even cause the junction premature breakdown before the inner electric field becomes high enough for impact ionization to generate the avalanche gain. Impact ionization in GaN has been studied by Dr. Razeghi's group, showing that the ionization coefficient is higher for holes [47]. Back-illuminated GaN *p-i-n* APDs and SAM APDs have been fabricated and then demonstrated for the high linear-mode avalanche gain and the Geiger-mode operation [28, 29, 35, 47]. However, two major issues exist for the back-illuminated GaN APDs: (1) UV-transparent substrates are needed for the back-illumination. Double-size polished sapphire is the best choice so far. Free-standing bulk GaN substrates cannot be used because of the strong UV absorption. The mismatch between the substrates and the epitaxial layers creates a lot of dislocations and dramatically increases the dark current. The dark current density of the back-illuminated GaN APDs is usually three orders of magnitude higher than that of GaN *p-i-n* APDs [26, 28, 29]. The large dark current density eventually limits the avalanche gain as well as the Geiger-mode performance. (2) Lower external quantum efficiency than front-illuminated GaN *p-i-n* APDs. While the substrate is UV-transparent, the *n*-GaN layer below the active region still absorbs UV light. Incident energy is further lost at the interfaces of these layers below the active region. The limited quantum efficiency eventually restricts the single-photon detection efficiency (SPDE).

Recently high-quality free-standing bulk GaN substrates with dislocation densities less than 10^6 cm^{-2} are commercially available for practical device applications. The dislocation density in the APD device can be dramatically reduced by growing the GaN epitaxial layers on native GaN substrates. GaN-based APDs grown on free-standing bulk GaN substrates have been

reported with ultra-low dark current [26], repeatable high avalanche gain [32] in the linear-mode with high device yield [32], and the reliable Geiger-mode operation [37].

In this thesis, the fabrication and characterization of GaN-based visible-blind UV *p-i-n* APDs grown on free-standing bulk GaN substrates will be presented. Several technical barriers and the possible solutions will be discussed in next section.

1.3 Technical barriers and possible solutions for III-nitride *p-i-n* APDs

In material growth, the development of III-nitride-based APDs was hampered by high dislocation density for epitaxial layers grown on foreign substrates such as sapphire and SiC. In the development of APDs, the dislocations often induce premature breakdown before the onset of device avalanching. Devices with premature breakdown can be observed and determined from several point-like light-emitting regions, which are called micro-plasma emissions. As the mesa size increases, the situation gets more serious as more defects may be included in high electric field region. This kind of premature breakdown is destructive for the *p-n* junction. To avoid micro-plasmas, most III-nitride-based APDs have been limited to small-area devices. To obtain low-dislocation-density materials, native substrates such as free-standing bulk GaN, which was not commercially available until recently may provide a possible solution. In this thesis, GaN *p-i-n* APDs are fabricated from structures grown on free-standing bulk GaN substrates to achieve low-noise and high-optical-gains. The epitaxial growth was done by Prof. Dupuis' group at GT.

In device fabrication, mesa etching for *p-i-n* diodes is a critical processing step. III-nitride device mesa etching techniques usually cannot avoid creating damage in the mesa sidewalls. Dry etching creates trap centers on the etched surface and may result in significant sidewall leakage-

currents in a wide variety of devices such as rectifiers, photodiodes, LEDs, LDs, and transistors. To reduce the mesa-etching-induced device degradation, surface passivation by plasma enhanced chemical vapor deposition (PECVD) is a commonly used solution. However, the PECVD passivation can only recover the etching-induced defects on the surface, leaving the material damage underneath the surface unrecovered [48]. In this thesis, two sidewall leakage reduction methods were studied. They are proven to be effective for sidewall leakage reduction. The reverse-biased diode leakage current can be suppressed by one to three orders of magnitude. These methods have been applied as standard fabrication modules for high-performance GaN *p-i-n* APDs presented herein. They are also have been used for the substrate treatment before epitaxy [49].

1.4 Thesis synopsis

Chapter 2 discusses the fabrication processing for GaN UV homojunction *p-i-n* APDs with a focus on the development of two sidewall leakage reduction methods for III-nitride device fabrication. First, a wet-etching surface treatment method were studied and an optimized process recipe was determined using the design of experiment (DOE) approach. Next, a double-mesa surface depletion technique will be discussed. Experimental results show that the first method can suppress the reserve-biased diode leakage current by at least one order of magnitude, and the second method can reduce the leakage current further by as many as three orders.

The characterization of the GaN visible-blind UV *p-i-n* APDs will be presented in Chapter 3. Spectral response, linear-mode avalanche gain, demonstration of the Geiger-mode

operation, current-voltage (I-V) characteristics, capacitance-voltage (C-V) characteristics, and noise performance will be discussed.

Chapter 4 will summarize the research in this thesis and highlight important device performance achievements.

CHAPTER 2 DEVICE FABRTICATION

Suppressing leakage current is an important issue for both the material growth and device fabrication of GaN *p-i-n* APDs and low-noise photodiodes. In material growth, the leakage current density is related to the dislocation density due to the lattice mismatch between substrates and epitaxial layers. Free-standing GaN bulk substrates are preferably used to minimize the strain-induced dislocations [50]. In device fabrication, the dry etching process to form the *p-i-n* mesa results in surface defects. These surface states at the etched sidewall typically cause increased leakage current and premature breakdown (micro-plasma). To reduce the sidewall leakage, a conventional method is to deposit a plasma-enhanced chemical vapor deposition (PECVD) passivation layer using SiO_2 or SiN_x [45]. However, this method requires tight process control on the interface strain properties, and the energetic plasma applied during the deposition may induce secondary surface damage. Moreover, the PECVD-deposited dielectric layer can only recover the etched surface but there are still etching damage underneath the surface which remains un-passivated [48].

To explore robust and effective sidewall leakage reduction methods, a wet-etching surface treatment technique and a double-mesa surface depletion technique were proposed and studied in this thesis. The first technique removes surface etching damage by wet-etching several layers of GaN atoms. In contrast with PECVD passivation, wet-etching surface treatment removes defects instead of recovering them. The second technique is only used for *p-n* junction devices. By forming a depleted ledge layer with a double-mesa structure, damage on the sidewall

can be electrically isolated by the high-resistive depletion region. Both methods are capable of reducing leakage paths in our study. Experimental results show that the *p-i-n* junction leakage current can be reduced by one to three orders using these methods compared with PECVD SiO_2 passivation. These methods have been applied for the GaN *p-i-n* APDs fabrication. The suppressed leakage current plays critical roles in achieving high avalanche gains in the linear-mode and the Geiger-mode for single photon detection. Low-noise photodiodes in the photovoltaic mode and the photoconductive mode are also achieved.

Another issue in device fabrication is the difficulty to form *p*-type GaN ohmic contacts. The problem comes mainly from the difficulty of achieving high *p*-type material doping in MOCVD growth. The optimization of *p*-type GaN/metal contact for a low specific contact resistance will be presented as well.

2.1 PEC surface treatment development

High-performance III-nitride devices require high-quality surfaces during the fabrication processing for low surface leakage current. Mesa etching is the main device processing step that determines the sidewall and material surface quality. Plasma-based dry etching methods such as inductively coupled plasma (ICP) and reactive-ion etching (RIE) often induce ion damage to the device surface as well as the mesa sidewall. Consequently, these methods may decrease device performance due to increased surface leakage current. Wet etching technique is an alternative to dry etching to reduce plasma-induced surface damage. Conventional chemical wet etching, such as buffered oxide etch (BOE) or HCl wet etching, does not work for high-quality III-nitride materials because of the chemical stability. Some groups have reported studies on

photoelectrochemical (PEC) etching [51-56] and/or ultraviolet-assisted wet etching [57-59] as alternatives to the plasma etching.

Wet etching in III-nitride materials still leaves two problems. First, the UV-assisted wet etching is a selective etching to *n*-type III-nitride materials [51]. The etching rate on *p*-type III-nitride materials is essentially low so it cannot be used to fabricate mesas on *p*-type materials. Second, typical UV-assisted wet etching tends to have a higher etching rate on sites where the defect density is high. The wet-etching techniques are typically used for defect density studies on *n*-type III-nitride materials rather than for achieving high-uniformity etching surfaces in device fabrication processing [60]. Recently, Balarge's group demonstrated the possibility of using a diluted $KOH/K_2S_2O_8$ solution to achieve binary etching on intrinsic, *p*-type, and *n*-type GaN epitaxial materials [57]. The low etching rate with such solutions not only provides tight control of the III-nitride devices fabrication but also reveals the possibility to use it as a useful surface treatment technique for APD processing. The efficacy of using this new wet-etching chemical system for the surface treatment on III-nitride minority carrier devices, however, has yet to be studied.

To develop a suitable wet-etching surface treatment process for III-nitride *p-n* junctions, an ICP dry etching is first used for *p-i-n* mesa etching. The etched *n*-type surface and the sidewall are then treated in a UV-assisted surface treatment to remove only a few mono-layers of III-nitride surface atoms. The carrier trap centers on the etched surface are removed to improve leakage current characteristics. In contrast to the conventional PEC etching, potassium persulphate ($K_2S_2O_8$) is used as the oxidant to remove the need for electrodes in the UV-assisted surface treatment step. To achieve a smooth surface morphology with reduced high-filed leakage

current, a set of design of experiments must be conducted by studying the correlation between UV illumination power, KOH concentration, and the $K_2S_2O_8$ concentration.

A three-factor two-level design of experiment (DOE) study was conducted to determine an optimal etching recipe [61]. Before wet etching, eight GaN samples grown on sapphire substrate were cut from a 2-inch wafer. They were mesa etched by an optimized BCl_3/Cl_2-based dry etching recipe in a STS ICP system. The etching depth was 1000 Å with an etching rate of 1000 Å/min. These etched samples were then used to study an optimal surface treatment with the electrode-less UV-assisted wet-etching technique. KOH concentration, $K_2S_2O_8$ concentration, and UV light power were three experimental variables for the surface treatment study, and were designed to a two-level variation: high level (H) and low level (L), respectively. This gives a total of eight different etching conditions in this DOE. An Oriel UV light source having a 1 kW mercury-xenon lamp was used to provide the UV illumination [62]. Each sample was randomly assigned to one of the eight etching conditions. Chemicals were freshly prepared in DI water just before each wet etching, and the experiments were done at room temperature. The detailed experiment parameters for the three factors DOE are listed in Table 2.1.

The etching time was set at 5 minutes. The percentage of surface roughness improvement before and after the surface treatment was used as the output response. Surface roughness (RMS in nm) was measured by atomic force microscope (AFM) before and after ICP etching. The positions of the AFM scan are recorded so that the same location could be analyzed for valid comparison. Each sample is surface-treated using one of the eight etching conditions and a post-wet-etching AFM scan is evaluated to determine the surface treatment effectiveness. The surface

morphology improvement is defined in Equation 2.1. The DOE and the responses on the changes in surface roughness are summarized in Table 2.2.

$$\Delta\text{RMS}(\%) = \frac{\text{RMS before wet etching - RMS after wet etching}}{\text{RMS before wet etching}} \tag{2.1}$$

Table 2.1. The experimental parameters for each level of the three factors in the DOE of the wet-etching surface treatment study.

	High level	Low level
KOH concentration	0.0005 M	0.00025 M
$K_2S_2O_8$ concentration	0.002 M	0.001 M
UV illumination power	900 W	600 W

Note: M = mole/liter. UV power is the reading of the lamp driver's electric power.

Table 2.2. The DOE table in the wet-etching surface treatment study and the summary of the experiment response.

#	UV	KOH	$K_2S_2O_8$	RMS (nm) before wet etching	RMS (nm) after etching	ΔRMS (%)
1	H	L	L	0.390	0.378	3.07
2	H	H	L	0.385	0.348	9.61
3	H	L	H	0.315	0.340	-7.93
4	H	H	H	0.272	0.349	-28.3
5	L	L	L	0.281	0.344	-22.41
6	L	H	L	0.302	0.227	24.83
7	L	L	H	0.311	0.336	-8.03
8	L	H	H	0.266	0.333	-28.94

In Table 2.2, some etching conditions result in worse surface roughness that corresponds to a negative value in ΔRMS, possibly due to aggressive etching and/or the presence of dislocation defects. With proper choices of etching conditions, however, smooth surface may be achieved. To study the correlation between processing variables, the main effect and their interactions are plotted in Figure 2.1 (a) and Figure 2.1 (b), respectively.

Figure 2.1 (a) is a set of plots showing the main effects of KOH concentration, $K_2S_2O_8$ concentration, and the UV illumination power for the surface roughness improvement in this bi-level DOE study. The data points are averaged for each level for parameters specified on top of each graph. The "L" level corresponds to "0" and the "H" level corresponds to "1" in each plot. It is observed that the $K_2S_2O_8$ concentration has a significant effect: lowering the $K_2S_2O_8$ concentration can improve the surface uniformity. The other two variables' influences however are not obvious in this plot. Figure 2.1 (b) is a set of plots showing the interactions between KOH concentration, $K_2S_2O_8$ concentration, and the UV power. Variables in the diagonal boxes indicate the parameters used in the x-axis of each column. The interactions with the variable indicated in the row are shown with solid circles for the "H" levels and solid squares for the "L" levels, respectively. It is shown that $K_2S_2O_8$ and KOH have significant interaction. KOH concentration is also significant but its effect varies with different $K_2S_2O_8$ concentration level. In etching conditions with a low $K_2S_2O_8$ concentration, a higher KOH concentration may yield smoother surface. On the other hand, if $K_2S_2O_8$ concentration is "high", a higher KOH concentration produces a rougher surface. Based on this DOE, an effective wet-etching-based surface treatment can be achieved with a $K_2S_2O_8$ concentration in the vicinity of "L" level and a KOH concentration around the "H" level. The UV illumination power however may not be a dominant factor.

Using the optimized wet-etching condition obtained from this DOE, one *n*-type GaN ICP-etched sample is surface treated and AFM scan pictures on the dry-etched surface before and after the wet-etching surface treatment are taken and shown in Figure 2.2 (a) and Figure 2.2 (b), respectively. The surface roughness is improved by ~75% after the surface treatment when

compared to the ICP-etched non-treated surface (with a dramatically RMS value reduction from 3.527 nm to 0.775 nm). In Figure 2.2 (a), some "spikes" were induced by dry etching because the etching rate varies near the material dislocations. They can act as surface leakage paths and may greatly degrade the device performance. But they are effectively removed by the surface treatment, as shown in Figure 2.2 (b). The comparison clearly shows the ability of the wet-etching surface treatment technique for effective surface morphology modification. Figure 2.3 shows 3D AFM images of etched mesa sidewall morphology from the same sample before and after wet-etching surface treatment. It is noted that the wet-etching surface treatment reduces the mesa sidewall taper from 200 nm to less than 100 nm, indicating a sharper sidewall as well as the removal of several layers of etching-damaged GaN atoms that may provide carrier trap centers. As a result, a smoother sidewall is also obtained. We have a provisional patent filed for this treatment technique[10].

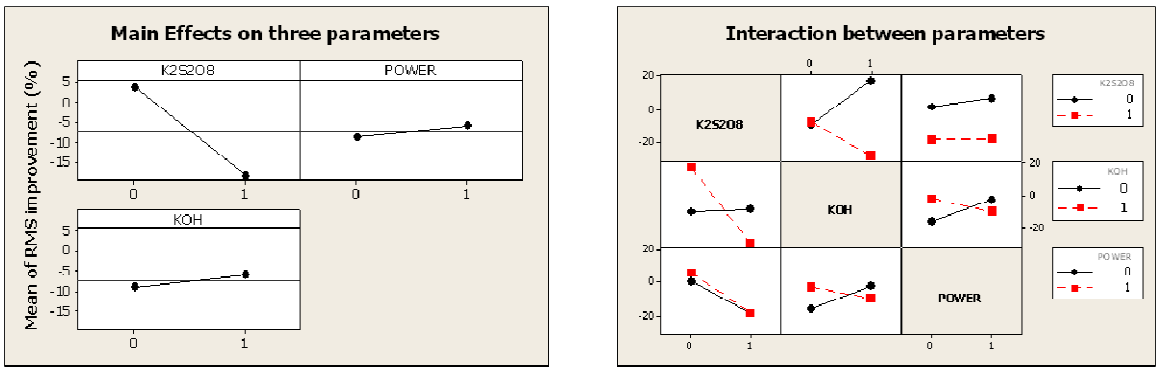

Figure 2.1. (a) Main effects of KOH concentration, $K_2S_2O_8$ concentration, and UV illuminated power for the surface roughness improvement (b) Interaction effects between KOH concentration, $K_2S_2O_8$ concentration, and UV illuminated power for the surface roughness improvement.

[10] "A Method of Manufacture of III-N Semiconductor Devices using Electrode-Less Photon-Assisted Wet Etching Techniques", GTRC ID No. 4185.

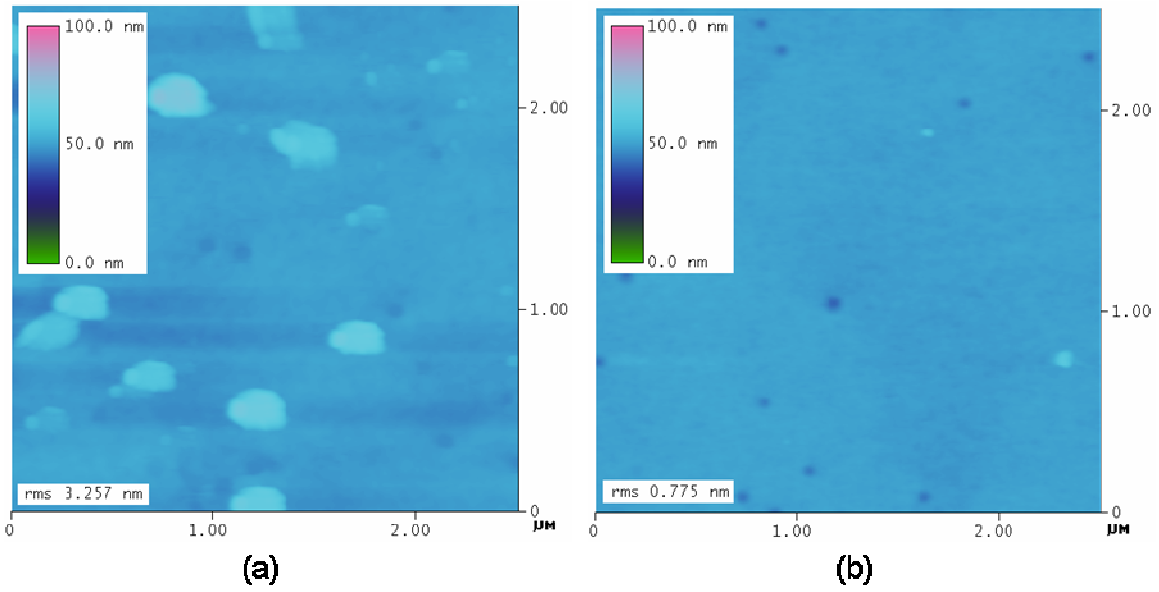

Figure 2.2. 2D AFM scan images showing an ICP-etched *n*-type GaN sample surface (a) before the wet-etching surface treatment and (b) after the wet-etching surface treatment.

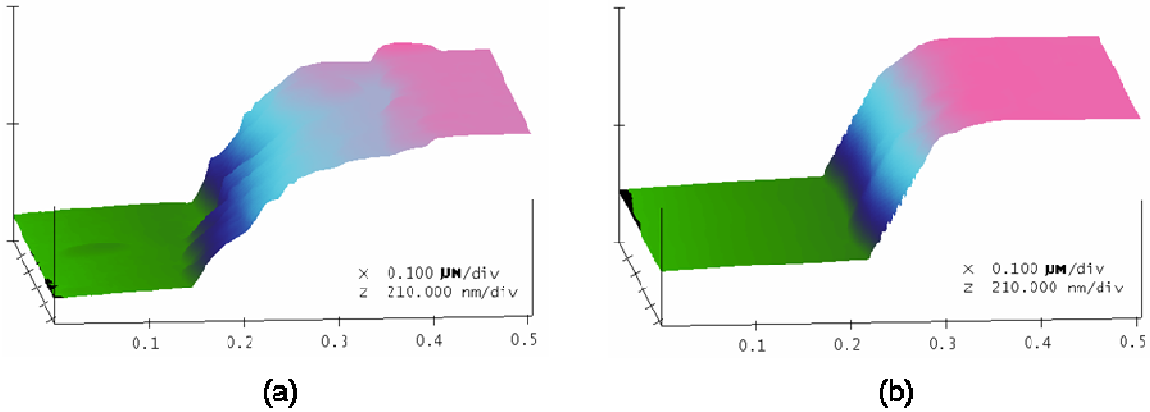

Figure 2.3. 3D AFM scan images of the etched mesa sidewall (a) before the wet-etching surface treatment and (b) after the wet-etching surface treatment. The rotation angle is 85 degree and the pitch angle is 10 degree for the 3D images.

To further study the efficacy of the sidewall leakage suppression due to the wet-etching surface treatment, GaN *p-i-n* diodes grown on SiC substrates (wafer ID: 1-0906-2) were fabricated and were surface treated. The reverse-biased I-V characteristics are compared with

those fabricated devices without the surface treatment. Typical reverse-biased I-V curves (leakage current in the dark condition) with various etching conditions are shown in Figure 2.4. With a proper surface treatment condition (Condition B in Figure 2.4) the leakage current in *p-i-n* diodes can be reduced by at least one order of magnitude. At the same time the device breakdown voltage extends to a higher value and catastrophic breakdown (shown in Condition A in Figure 2.4) is not observed. Therefore, the optimized wet-etching surface treatment technique is useful for the fabrication of GaN *p-i-n* APDs which are reverse-biased near breakdown [30, 49]. This technique has been also applied for high-performance III-nitride high electron mobility transistor (HMET/HFET) fabrication to eliminate interface charge [30, 49].

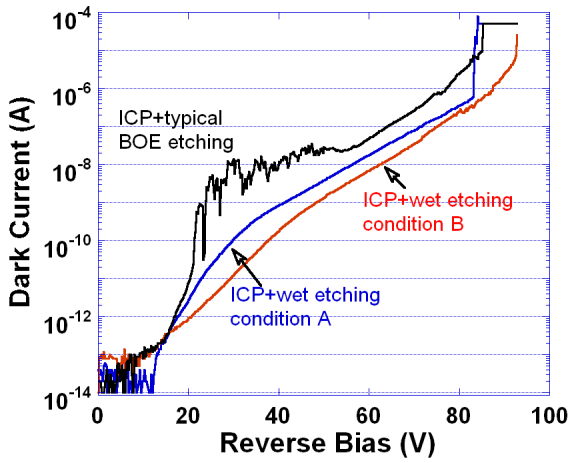

Figure 2.4. The reverse-biased leakage current comparison among fabricated GaN (SiC substrates) *p-i-n* diodes with different wet-etching surface treatment conditions.

2.2 A surface depletion technique using a double-mesa structure

The wet-etching surface treatment technique discussed in the previous section can provide a promising solution to suppress the sidewall leakage by at least one order of magnitude. In contrast to the conventional PECVD passivation method, this technique is able to remove the trap centers not only on but also underneath the plasma-damaged surface. However, as shown in the last section, the condition control of this surface treatment technique is also tight and needs to be carefully optimized, which potentially reduce the processing reliability. If the chemical concentration is too low, the dry-etching-surface damage on the device sidewall is usually difficult to be fully removed by surface treatment techniques. On the other hand, if the treatment recipe is too aggressive, the removal rate will be not uniform, depending on the dislocations distribution, and even more defects may be induced by the wet etching. For high-performance, high-yield III-nitride devices operating at high power and high voltage conditions, a more effective methodology to fully eliminate the inevitable etching-induced leakage paths would be highly desired.

To achieve this goal, another effective sidewall leakage suppression technique is studied using a built-in *p*-*n* junction surface depletion layer to suppress the sidewall leakage current for mesa-etched bipolar devices. This is similar to the ledged structure in the heterojunction bipolar transistor (HBT) [63]. Using a double-mesa structure (as shown in Figure 2.5 (a)), a thin layer of the *p*-type III-nitride layer is left on the edge of the second mesa using a conventional ICP etching to form a surface depletion layer. This depletion layer forms a highly resistive region that can electrically isolate the sidewall defects from the *p*-metal contact. Compared to traditional single mesa etching (Figure 2.5 (b)) the sidewall damages can therefore be effectively suppressed

even though no surface treatment is applied to recover the carrier trap centers. To study the electric field distribution in this structure, *p-i-n* diodes w/ and w/o the ledged structure are modeled in ISE-TCAD and the results are shown in Figure 2.6 [64]. It is apparent that the double-mesa structure can reduce the electrical field on the sidewall of the *p-i-n* diode effectively. A weaker electrical field near the sidewall was observed and hence it may help suppress the leakage current for a given reverse bias. As a result, the device breakdown can be extended and APDs may be fabricated in a more robust fashion.

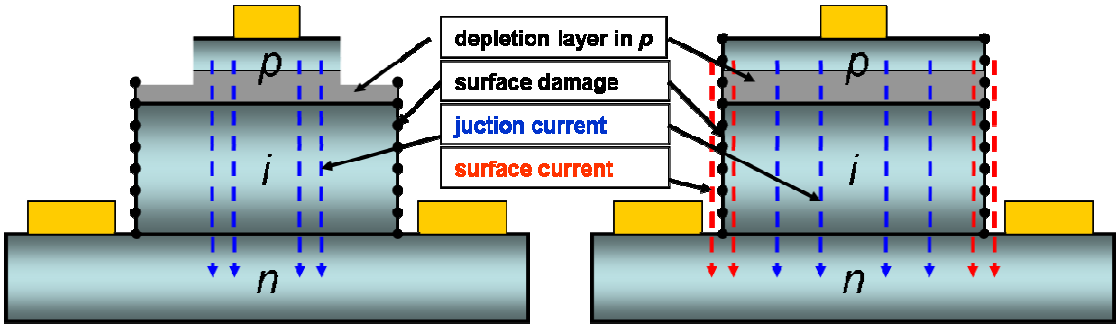

(a) (b)

Figure 2.5. Schematic drawings of III-nitride mesa etched diodes with (a) a double-mesa scheme with a surface depletion layer (b) a single-mesa scheme.

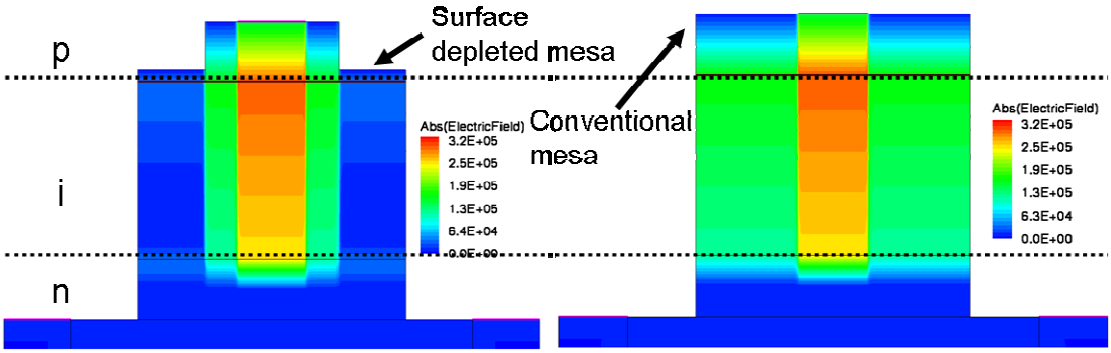

(a) (b)

Figure 2.6. Simulated electric field distribution using ISE-TCAD for (a) a single- and (b) a double-mesa structure III-nitride *p-i-n* diode.

Double-mesa structure GaN *p-i-n* diodes (grown on SiC substrates) were fabricated. Their performance is compared with the single-mesa structure devices without any post-ICP-etching surface treatment, as well as the single-mesa structure devices treated using the optimized wet-etching surface treatment condition from Section 2.1. All the three samples have the same GaN *p-i-n* layer structures and doping levels, and are grown on the same SiC substrates (wafer ID: 2-0906-2) in the same metalorganic chemical vapour deposition (MOCVD) growth batch. Typical reverse-biased I-V curves (leakage current in the dark condition) are shown in Figure 2.7. Both Sample A and B are fabricated using ICP mesa etching for a typical single-mesa diode structure. After mesa etching Sample A is only treated in BOE to remove the etching mask. The optimized wet-etching surface treatment recipe obtained in Section 2.1 is applied to Sample B to further recover the dry-etching induced material damages. A double-mesa structure is formed on Sample C using ICP etching without the surface treatment. It is shown that the double-mesa structure surface depletion technique reduces the leakage current by three orders of magnitude, which is one order better than the result of optimized wet-etching surface treatment. A comparison table of sidewall-leakage-reduction methods, including the PECVD passivation, the wet-etching surface treatment technique, and the double-mesa structure surface depletion technique, is presented in Table 2.3.

In this thesis, the wet-etching surface treatment technique was used in the fabrication of the first batch of single-mesa GaN homojunction *p-i-n* APDs. They exhebit record optical avalanche gain > 10^5, which will be presented in Section 3.1.3 (Wafer ID: 1-0907-5). This method was also used for HFET fabrication to improve the device performance [61].

The double-mesa structure surface depletion technique was applied to the fabrication of the second batch of double-mesa GaN homojunction *p-i-n* APDs, showing the Geiger-mode operation with single photon detection efficiency (SPDE) of 1% at 265 nm. Ultra-low noise performance is also achieved when photodiodes biased in the photoconductive mode or photovoltaic mode. In cases where a passviation layer is needed for electric isolation purposes, a spin-on Benzocyclobutene (BCB) is applied as well, which will be described in Section 2.4.

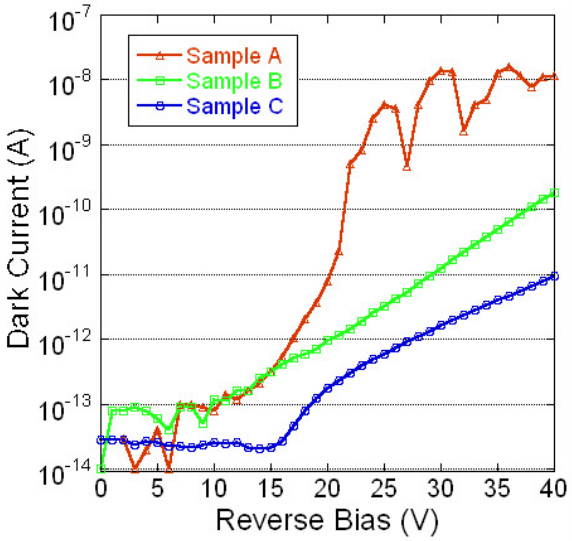

Figure 2.7. The comparison of reverse-biased leakage current of ICP-mesa-etched GaN *p-i-n* diodes. Sample A: BOE surface treatment only, Sample B: Optimized wet-etching surface treatment and Sample C: ICP-mesa-etched double-mesa structure GaN *p-i-n* diodes.

Table 2.3. A summary of the process and conclusions of the three sidewall-leakage-reduction methods studied in this thesis.

Solutions	Approaches	Advantages	Disadvantages
PECVD passivation	PECVD-grown SiN_x or SiO_2 for sidewall passivation	A commonly used method to recover etching damages	Tight process control is needed
A wet-etching surface treatment technique	A UV-enhanced electrode-less wet-etching surface treatment	A simple and effective method to remove surface damages	Surface damages are difficult to be fully removed
A double-mesa surface depletion technique	A sidewall leakage suppression technique using a built-in *p-n* junction surface depletion	A method to reduce the electric field across the sidewall	One more dry etching is needed

2.3 The *p*-type and *n*-type GaN ohmic contact study

Ohmic contact with low contact resistance is required on both *p*-GaN/metal and *n*-GaN/metal contacts for high qualify *p-n* junction-based GaN devices, such as photodiodes, LEDs, LDs, and HBTs [65]. For APDs or photodiodes, a better ohmic contact helps improve the quantum efficiency. It is also very important for the Geiger-mode operation to reduce the voltage drop at the metal-semiconductor interface (more details in Section 3.1.3). However, because of the relatively low Mg-doping in *p*-type III-nitride materials as well as the large bandgap energy, achieving low-resistance *p*-type ohmic contact is a challenge for III-nitride device fabrication. To obtain the ohmic contact, high-work-function metals, such as Ni (5.15 eV), Pd (5.12 eV), and Pt (5.65 eV), are commonly used as the contact layer, followed by Au or Pt as the protection layer from oxidation. Annealing is applied to accelerate the diffusion between metal and semiconductor and form metal alloys. The metal-semiconductor barrier is reduced and the ohmic profile with lower contact resistance is achieved. Numerous papers have been reported about this

approach [66-81]. In this work, Ni/Au or Pd/Au for *p*-GaN ohmic was also studied for GaN *p-i-n* APD development, but ohmic contact is not achieved. The reason may be the higher material qualify and lower dislocation density on the epitaxial GaN materials grown on native GaN substrates.

Recently Ni/Ag based *p*-GaN ohmic contact followed by annealing in O_2 or air has been widely studied and reported, showing the improved ohmic profile, lower specific contact resistance (ρ_c) and higher optical reflectivity [75, 82-95]. The Ni layer can improve the metal adhesion and provide a large work function, and the NiO film can also help the formation of *p*-GaN ohmic contact [68]. Ga atoms have obvious diffusion into the metal layers because of the strong interactions between O and Ga [85]. The thermally stable Ag-Ga solid solution is then formed at the interface between the *p*-GaN surface and metals [85]. Consequently, many Ga vacancies are generated near the *p*-GaN surface and the hole concentration greatly increases. The schottky barrier is reduced and the ohmic contact can be easily achieved. In this thesis, a Ni/Ag/Ni/Au scheme is studied as an ohmic contact layer to *p*-GaN for UV APD development. The optimized metallization conditions as well as results comparison with Ni/Au and Pd/Au approaches will be presented.

The transmission line measurement (TLM) is used for ohmic contact analysis for device characterization in this study. The TLM method employs an etched mesa, and metal contact pads are subsequently deposited on the top of the mesa as shown in Figure 2.8 (a). Figure 2.8 (a) illustrates some parameters used in the measurements and calculations. L is the length of rectangular contact (μm), Z is the width of rectangular contact (μm), and d is the space between neighbor contacts (μm). The purpose of the mesa is to confine the current flow to the gap

between contact pads. An important parameter that indicates the quality of the ohmic contact is the specific contact resistance (SCR, ρ_c), also called the contact resistivity. SCR equals to the product of the contact resistance and the effective area of the contact through which current flows. By measuring the resistances between neighboring contact pads and plotting them as a function of their spaces, the contact resistance and the semiconductor's sheet resistance can be extrapolated, as shown in Figure 2.8 (b).

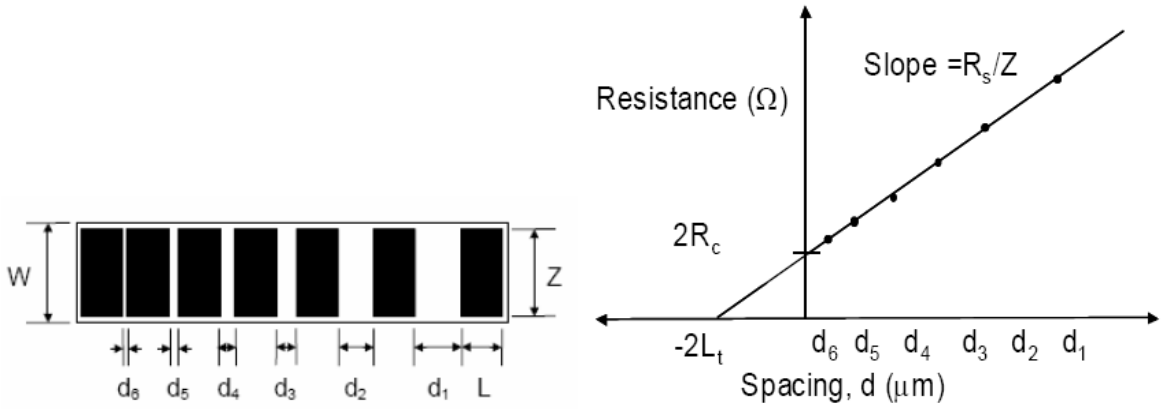

(a) (b)

Figure 2.8. (a) Plain view of the TLM pattern showing the semiconductor mesa with dark metal pads (b) Plot of measured resistance versus contact spacing [96].

The sheet resistance of the semiconductor can be calculated from the slope: R_s = slope × Z. As shown in Figure 2.8 (b), the x-intercept is twice the transfer length, $2L_t$. The transfer length is defined as the distance from the edge of the contact pad to the point at which the contact voltage is 1/e of its maximum value. The y-intercept gives twice the contact resistance, $2R_c$. The effective contact area is defined as the product of the transfer length and the contact width: $L_t \times Z$. The SCR can then be calculated from the following equations: $\rho_c = L_t \times Z \times R_c$.

Evaporated Ni/Ag/Ni/Au (50 Å/500 Å /50 Å /100 Å) metal stack is used as the *p*-GaN ohmic contact. The role of Ni/Ag in *p*-GaN ohmic contact was discussed earlier. The gold layer

acts as a protective layer from oxidation in the processing. The second Ni layer is a diffusion blocking layer between the silver and the gold layers. The optimized annealing condition is 500^{o} C for 1 minute in air using a rapid thermal annealing (RTA) system. For comparisons, conventional Ni/Au (50 Å/50 Å) and Pd/Au (200 Å/200 Å) metal contacts were also evaporated and annealed. For ohmic contact study, I-V curves between two 40 µm × 80 µm pads with a space of 4 µm are used to check the linearity as shown in Figure 2.9. Ohmic contact is achieved with Ni/Ag/Ni/Au stack with a linearity of 0.997. The curve is slightly nonlinear at zero bias perhaps because the carrier concentration is still not high enough in the *p*-GaN layer. To calculate its SCR the TLM method is used as shown in Figure 2.10. By linear regression, the calculated sheet resistance (R_s) and SCR (ρ_c) are 102.0 KΩ/□ and 2.15 x 10^{-3} Ω-cm^2, respectively. The SCR is low enough for the successful fabrication of GaN UV APDs.

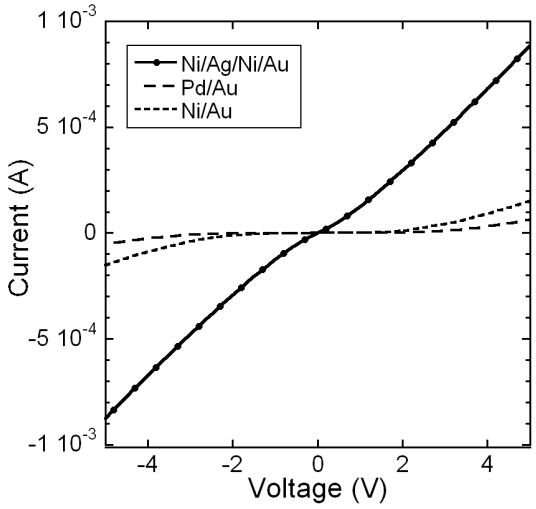

Figure 2.9. I-V curves between two 40 µm x 80 µm pads with a space of 4 µm for *p*-GaN metal contact with Ni/Ag/Ni/Au, Pd/Au, and Ni/Au.

Compared to *p*-GaN ohmic contact, a low resistive ohmic contact is much easier to be achieved on *n*-GaN layers. Figure 2.11 shows the TLM measurement results of a *n*-GaN ohmic

contact. Evaporated Ti/Al/Ti/Au (300 Å/500 Å /300 Å /500 Å) metal stack is used and it is shown that no annealing is needed on as-etched *n*-GaN surface. The calculated sheet resistance (R_s) and SCR (ρ_c) are 34.22 Ω/□ and 7.66 x 10^{-5} Ω-cm^2, respectively.

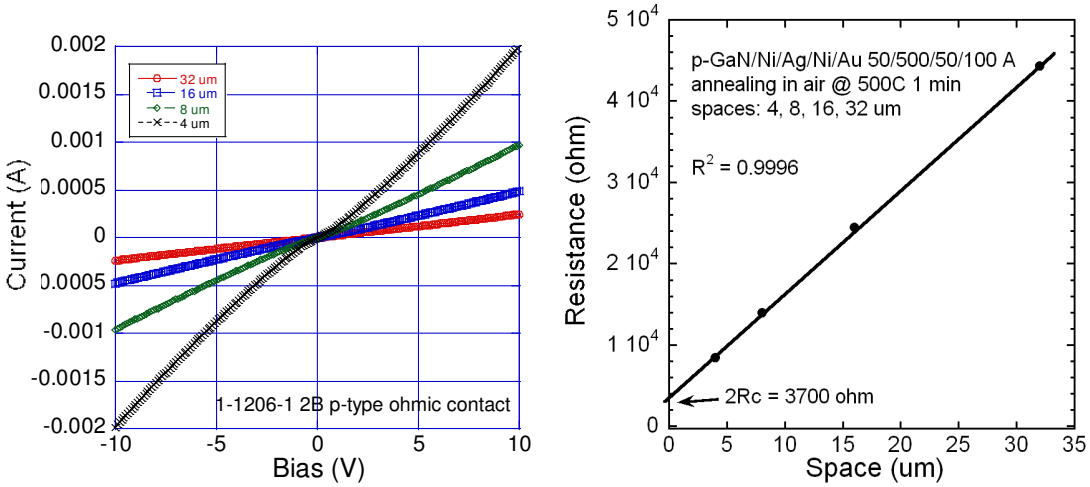

(a) (b)

Figure 2.10. (a) I-V curves between 40 µm x 80 µm pads with different spaces for *p*-GaN metal contact using Ni/Ag/Ni/Au (b) Plot of measured resistance versus contact spacing.

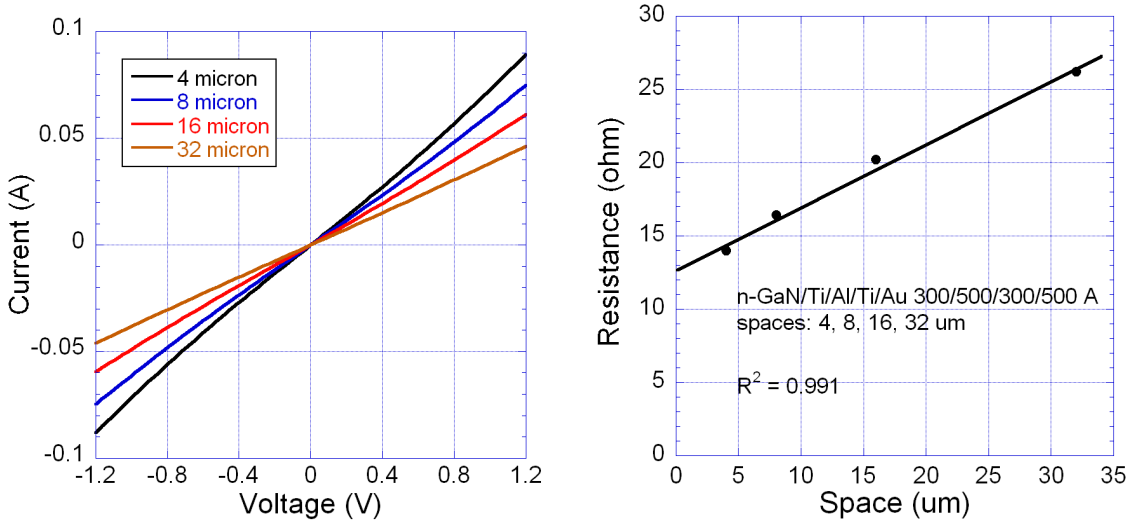

(a) (b)

Figure 2.11. (a) I-V curves between 40 µm x 80 µm pads with different spaces for *n*-GaN metal contact using Ti/Al/Ti/Au (b) Plot of measured resistance versus contact spacing.

2.4 Fabrication of GaN UV *p-i-n* APDs

The GaN epitaxial materials used in the research of this thesis are grown by MOCVD system equipped with a Close-Coupled Showerhead (CCS) growth chamber in Prof. Dupuis' group at GT. Detailed growth techniques were described in [26]. Typical epitaxial layers are grown on an *n*-type free-standing bulk GaN substrate with a nominal electron concentration of ~1×10^{18} cm^{-3}. The GaN UV APD consists of a 2.5-μm thick *n*-GaN:Si layer (n = 5×10^{18} cm^{-3}), followed by a 280-nm thick unintentionally doped (estimated n = 5×10^{16} cm^{-3}) GaN layer, a 100-nm *p*-GaN:Mg layer, and a 20-nm *p*++ cap layer, to form a homojunction *p-i-n* diode. The approximated free-hole concentration is ~ 1×10^{18} cm^{-3} based on previous growth calibrations [97]. The thickness variation of GaN APD samples used in this study is list in Table 2.4.

Table 2.4. Material layer structures of different GaN APD samples used in this thesis.

Sample #	*p*++ (nm)	*p* (nm)	*i* (nm)	*n* (nm)	substrate
1-0907-5	20	100	280	2500	GaN
1-1206-1	20	100	300	2500	GaN
2-1283-1	20	100	300	2500	GaN
2-1283-6	20	100	300	2500	GaN

The device fabrication flow chart is shown in Figure 2.12. Positive two-layer photoresist (S1813/LOR10B) and a Karl Suss MJB-3 aligner are used for photolithography. The fabrication starts with a two-mesa low-damage etching using a BCl_3/Cl_2 based inductively coupled plasma (ICP) etching tool (STS Multiplex System). Evaporated SiO_2 followed by a typical lift-off process is used as the etching mask to protect the *p*-mesa during the ICP etching. The first mesa-etching step keeps a thin *p*-type layer (approximately 30 nm in thickness) left on the top of the *i*-layer to form the surface depletion guard ring (or ledge) [64]. After the first mesa formation, the

SiO_2 mask is etched away by BOE. Then SiO_2 etching mask is patterned again for the second mesa etching. The second etching is a deep mesa-etching to expose the *n*-GaN layer for front-side *n*-type ohmic contacts.

Afterwards, the *p*-contact photolithography patterning and the E-beam evaporation of a 50/500/50/100 Å Ni/Ag/Ni/Au metal stack are performed. The *p*-contact metal is then lifted off and annealed in a rapid thermal annealing (RTA) system to form the *p*-type ohmic contact. The annealing condition is 500^{o} C for 1 min in regular air. The *n*-contact metal lithography is the following step. A 300/500/300/500 Å Ti/Al/Ti/Au metal stack is formed by E-beam evaporation followed by a lift-off process. The *n*-contact is ohmic as deposit.

The devices are then passivated with spin-on Benzocyclobutene (BCB) (Dow Chemicals, Inc. 3022-35). One-hour hard baking in vacuum oven at 250^{o} C is required to make the BCB film solid. After baking, the final thickness of the BCB passivation layer is about 8000 Å. Another photolithography is applied to define the via holes patterns and an ICP etching is used to open these via holes on top of *p*- and *n*-metal with hard-baked photoresist (S1813) as the etching mask. Finally, a thick Ti/Au layer is E-beam evaporated to form wire-bonding pads. SEM pictures of completed devices (wafer ID: 1-0907-5) are shown in Figure 2.13.

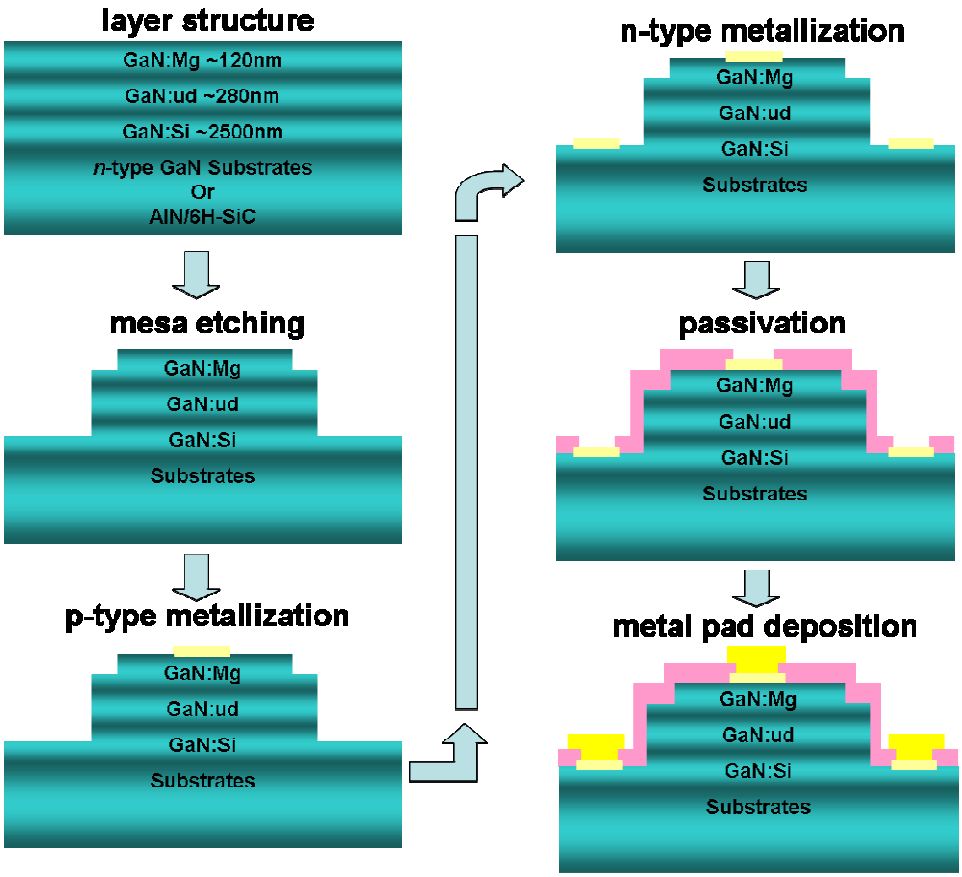

Figure 2.12. The fabrication process flow chart for GaN homojunction *p-i-n* UV photodiodes.

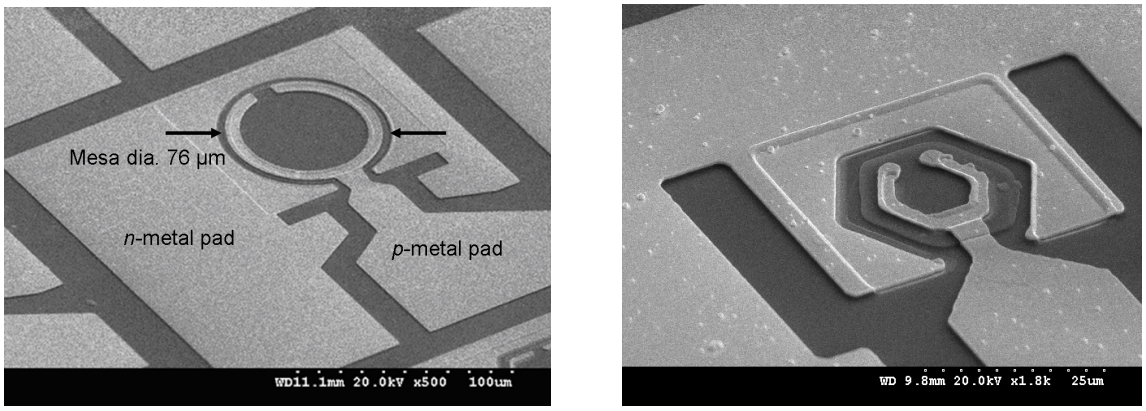

(a) (b)

Figure 2.13. SEM pictures of a fabricated (a) circular 76-μm-diameter (4536 μm^2) GaN UV *p-i-n* APD and (b) hexagonal 43.3 μm^2GaN UV *p-i-n* APD.

CHAPTER 3 DEVICE CHARACTERIZATION

3.1 Performance evaluation of GaN UV *p-i-n* avalanche photodiodes

The fabricated GaN visible-blind UV *p-i-n* APDs are characterized using an on-wafer DC probe station with a 50-μm-diameter UV fiber mounted on a micromanipulator. The DC probe station is located in a Faraday cage to reduce the influence of environmental noise. The light source is a Newport Apex Illuminator with a 150 W Oriel xenon (ozone-free) lamp, which can provide light illumination from 200 nm to 2400 nm with stable output. A Newport Cornerstone 260 monochromator system is used to provide single-wavelength optical signals that are coupled into the UV fiber and illuminated on the APDs from the top side of the wafer. The incident optical power is monitored using a calibrated Si-enhanced UV detector (Hamamatsu Inc. S2281-04). The device performances including spectral response, dark current, and linear-mode avalanche gain are evaluated and will be discussed in detail in the following sections.

3.1.1 Spectral response

Figure 3.1 shows a schematic drawing of the spectral response measurement system for this study. An optical chopper system is attached to the output window on the Newport Apex Illuminator to modulate the illumination light with a frequency of 100 Hz (for the signal recovery with a lock-in amplifier). Then the modulated illumination light goes into a ¼-m Cornerstone 260 monochromator system for the optical wavelength selection. The 1200 l/mm holographic grating (Newport 74162) in the monochromator has the resolution of 0.10 nm with a

primary wavelength region from 180 nm to 650 nm. After the wavelength selection the output from the monochromator can be considered as modulated (100 Hz) single-wavelength light. The single-wavelength modulated optical signal is then split by a 50/50 UV-VIS beam splitter. One half of the light is detected by a UV-enhanced Si photodetector for optical power monitoring. The other half of the light is coupled into a 50-µm-diameter UV fiber using a one-inch UV focus lens. The other end of the UV fiber is mounted to a micromanipulator and placed on top of the optical window of APDs under testing. To fairly evaluate the responsivity of the fabricated APDs, 100-µm-diamater devices are tested and the fiber end is located as close to the devices as possible so all the light can be collected. An SRS 830 lock-in amplifier is used to detect the APD photocurrent. The monochromater and the lock-in amplifier are controlled by a computer with a GPIB interface. An HP VEE program is used to control the instruments for data acquisition.

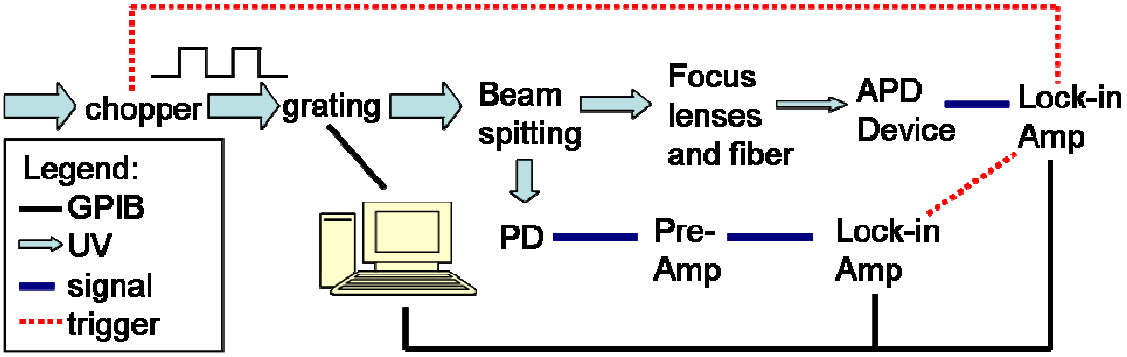

Figure 3.1. The illustration of the spectral response measurement system.

Figure 3.2 (a) shows the room-temperature bias-dependent responsivity of a fabricated 100-µm-diameter APD grown on free-standing bulk GaN substrates (wafer ID: 1-1206-1). The device has a breakdown voltage of 98 V with no micro-plasma observed on the sidewall. A zero-biased responsivity of 143 mA/W peaks at λ = 364 nm (3.41 eV) with a cutoff wavelength at 380

nm (3.26 eV). The zero-biased responsivity is higher than most of the published III-nitride APDs and photodiodes [27-29, 33, 35, 38-40, 42]. A higher responsivity is expected if a thinner top *p*-GaN layer (< 100 nm) is used. On the other hand, a thicker top *p*-GaN layer would be required to suppress the tunneling effect which can dramatically increase the dark current near breakdown [20]. To further enhance the responsivity an recessed optical window can be used after device fabrication [22].

Bias-dependent external quantum efficiency (EQE) curves of the fabricated APD are shown in Figure 3.2 (b). Under a bias with unity gain (~ 60 V), EQEs are 25.8%, 29.0% and 55.9% at 265 nm, 280 nm and 360 nm, respectively. The peak value is 57.6% at 364 nm at 60 V. With an increase in the reverse biases, the responsivity and EQE peaks shift slightly from 364 nm to near 370 nm due to the Franz-Keldysh effect. The increase of responsivity and EQE for reverse biases beyond 60 V corresponds to the carrier impact ionization in the *i*-layer. Significant avalanche photocurrent gain is observed in these *p-i-n* APDs when the reverse bias is greater than 80 V.

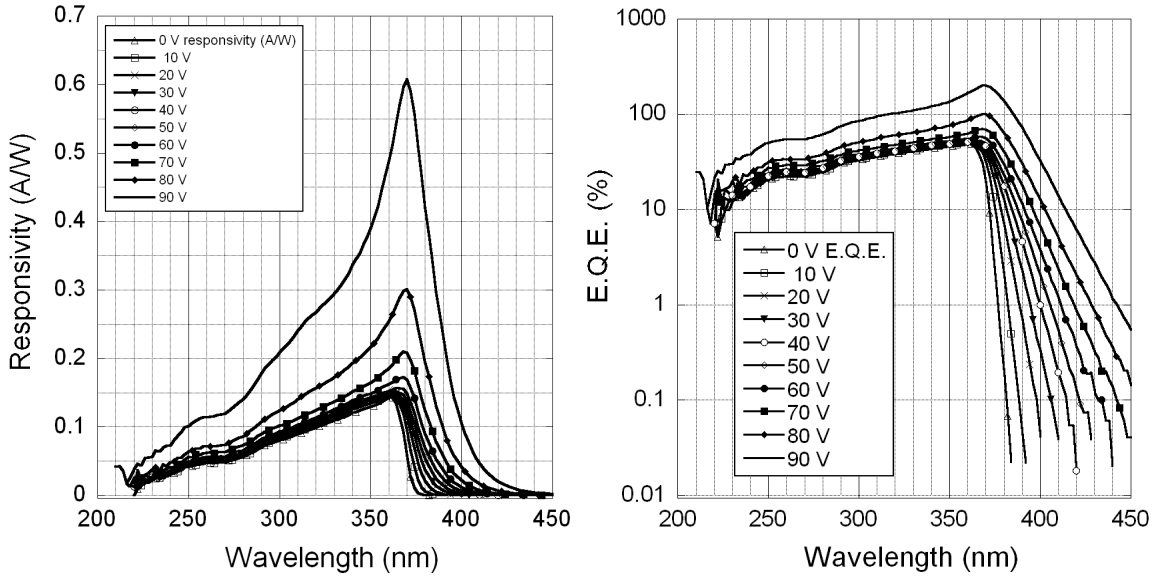

(a) (b)

Figure 3.2. (a) Room-temperature voltage-dependent photocurrent spectral response of a fabricated 100-µm-diameter GaN *p-i-n* APD (b) The room-temperature voltage-dependent external quantum efficiency (EQE) curve of the same device.

In addition, the absorption band shows significant broadening and red shifting at higher reverse biases, indicating that the depletion region extends into the doped layers because of the relatively low free-carrier concentrations. This phenomenon can be understood schematically in Figure 3.3 [30]. Since the UV light is illuminated from the top of the mesa, photons are absorbed through both band-to-band transitions and acceptor-state absorption in the *p*-type layer (absorption paths (1) and (2)). In addition to the band-to-band tunneling assisted absorption in the depletion region (absorption paths (3) and (4)) the acceptor-to-conduction-band absorption in the depleted *p*-GaN layer becomes significant due to the large number of ionized deep-level acceptor states (absorption path (5)). This situation is different from most lower-bandgap *p-i-n* diodes where the depletion region can be well-confined in the intrinsic layer due to the light *p*-

type doping. As a result, electrons at the acceptor states further induce significant red-shifting at the absorption edge due to increased electric field in the depleted *p*-GaN layer.

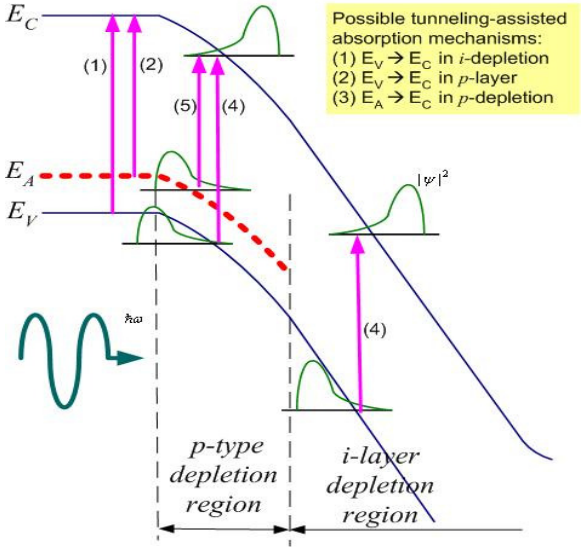

Figure 3.3. A schematic drawing showing possible mechanisms responsible for the band edge absorption spectrum red-shift.

3.1.2 C-V characterization

Shown in Figure 3.4 is a measured reverse-biased small-signal capacitance-voltage (C-V) curve of a fabricated GaN *p-i-n* APD in the dark condition. The corresponding depletion width curve is also included in this Figure. The mesa area of the device under test is 3161 μm^2. The C-V measurement is carried out in an HP 4284 LCR meter with a maximum reverse bias of 40 V at a signal frequency of 1 MHz. The capacitance reduces monotonically with the increased reversed bias, indicating that the depletion width of the *p-i-n* APDs may not be effectively confined within the intrinsic layer. It may extend in the *p*-type region as the reverse bias increases due to low *p*-doping, which is consistent with our photoresponse observation. Under a bias of - 40 V, the calculated depletion region is around 320 nm. Considering that the epitaxial *i*-layer is 280 nm

and the *n*-layer's carrier concentration is much higher than that of the *p*-layer, so the depletion width in the *p*-layer is 40 nm. The *p*-layer total thickness is 100 nm, so the *p*-GaN layer is not fully depleted at – 40 V.

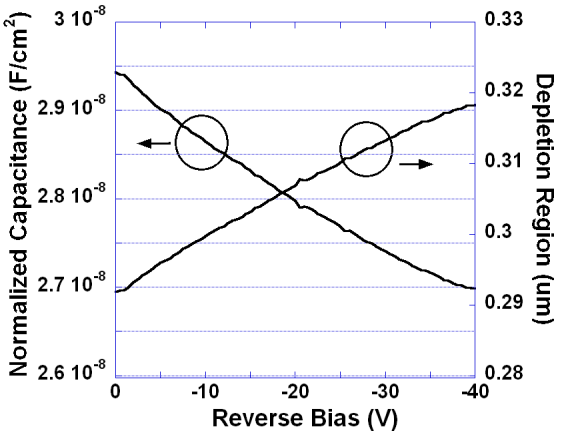

Figure 3.4. Typical small-signal capacitance and equivalent depletion region curves of GaN *p-i-n* APDs grown on free-standing bulky GaN substrates. The test frequency is 1 MHz and the device under test has a mesa area of 3161 μm^2.

3.1.3 Linear-mode avalanche gain

The DC I-V characteristics of the fabricated GaN *p-i-n* APDs are characterized using an on-wafer probe station and a Keithley 4200 semiconductor characterization system with low-current preamplifiers. The same illumination and wavelength selection system for spectral response measurement is used for photoresponse measurement. In this case, the illumination light is not chopped. There is an additional smaller metal shielding for the probe station to block other possible background UV illumination.

To evaluate the performance of the GaN visible-blind UV *p-i-n* APDs working in the linear-mode, the fabricated devices are reverse-biased near the avalanche breakdown region in both dark and UV illuminated conditions. Typical reverse-biased I-V characteristics including

dark current, photocurrent and avalanche gain are shown in Figure 3.5. Figure 3.5 (a) is for 280-nm illumination and Figure 3.5 (b) is for 340-nm illumination. The device under test has a diameter of 76 μm. In the dark condition, the leakage current density is below 10 nA/cm^2 up to -10 V. The breakdown voltage of the *p-i-n* APD is 92.3 V (or, equivalently, 2.6 MV/cm). The increase of the leakage current at higher reverse bias is attributed both to the bulk dislocation defects and surface states. The thickness of the depleted *p*-layer region is calculated theoretically and is verified by capacitance-voltage measurements with an LCR meter up to -40 V. With UV illumination, the photocurrent stays approximately constant up to 60 V before the impact ionization effect starts to significantly affect the current flow. The unity photocurrent $I_{ph(unity)}$ and dark current $I_{dark(unity)}$ are evaluated by taking the averaged photocurrent between 0 and 60 V under illumination. The avalanche gain (M) is calculated using Equation 3.1.

$$M = \frac{I_{ph} - I_{Dark}}{I_{ph(unity)} - I_{dark(unity)}} \tag{3.1}$$

As shown in Figure 3.5, an avalanche gain > 10^4 is achieved at 92.2 V (See the insets) for both 280-nm illumination and 340-nm illumination. Figure 3.6 shows a histogram of the avalanche gains distribution for 40 different-sized GaN *p-i-n* APDs measured across an 8 × 8 mm^2 GaN wafer piece. The working device is defined as a device with an avalanche gain of greater than 10^4. As shown in the graph, 75% of devices under test (DUT) shows avalanche gains > 2500 and 55% of the DUT shows avalanche gains >10^4 with a maximal gains > 35000. The results also show that devices with smaller mesa sizes have higher possibility to achieve higher avalanche gains, indicating the epitaxial growth-induced defects may still play a critical role for further device performance improvement.

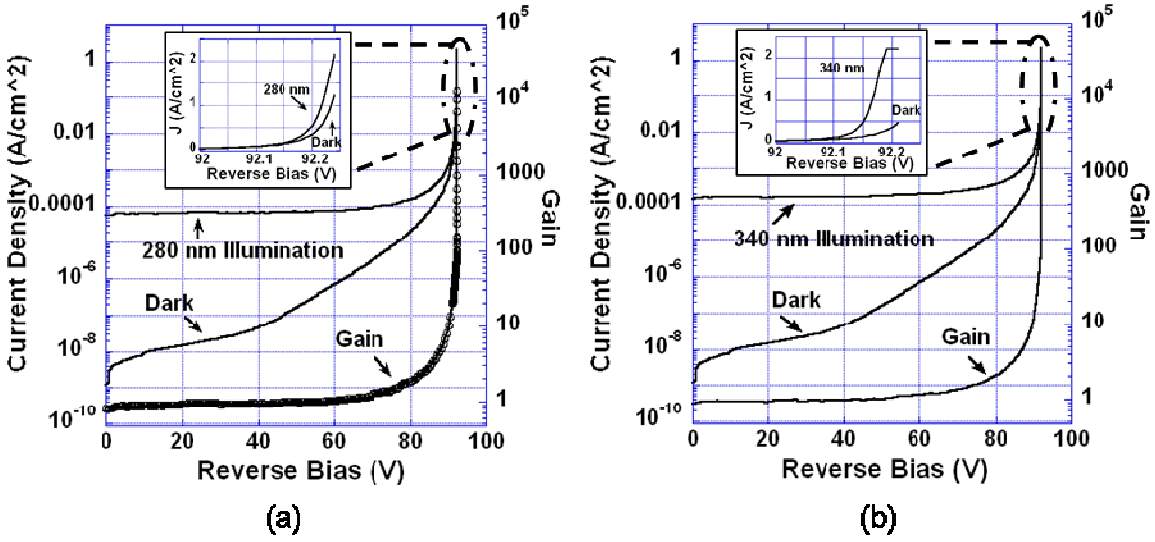

Figure 3.5. Reverse-biased I-V characteristics and the corresponding avalanche photocurrent gain of a fabricated 76-µm-diameter GaN *p-i-n* APD with and without UV light illumination: (a) 280-nm illumination, (b) 340-nm illumination.

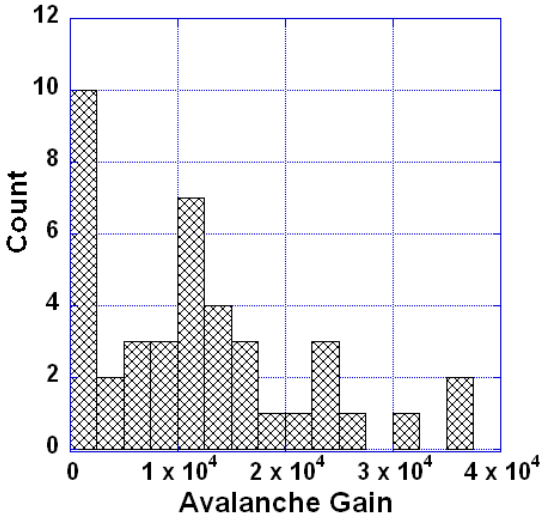

Figure 3.6. A histogram showing a distribution of avalanche photocurrent gain based on 40 GaN *p-i-n* APDs measured across an 8 x 8 mm^2 GaN wafer piece.

In the same sample, one smallest APD with the size of 570 um^2 shows a record avalanche gain > 10^5 at the reverse bias of 92 V with λ = 360 nm. This value is among the highest

avalanche photocurrent gain for III-nitride-based APDs reported to date. The I-V characteristics and corresponding avalanche gain curve of this device are shown in Figure 3.7.

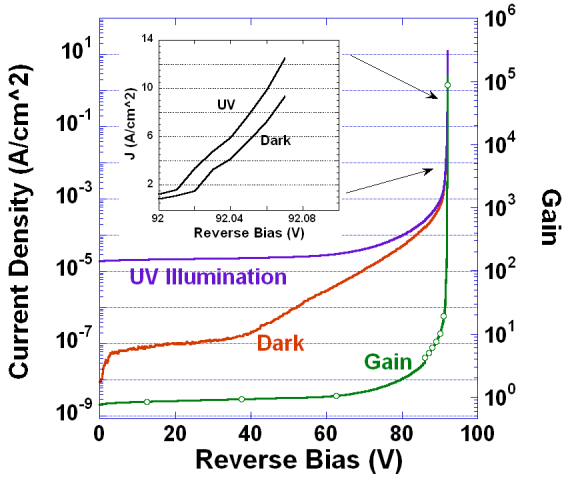

Figure 3.7. Reverse-biased I-V characteristics of a fabricated 570-μm^2 GaN *p-i-n* APDs with record avalanche gain > 10^5 at λ = 360 nm.

3.1.4 Geiger-mode operation

For the Geiger-mode operation, an APD is connected with a quenching circuit for the single photon detection [98]. The device is biased above avalanche breakdown waiting for an avalanche event. When an avalanche event is initiated by a photo-excited carrier or a thermally-excited carrier (dark count) the device current increases until reach the current limit of the external circuit. This avalanche event is recorded by a counter and the quenching circuit resets the bias of the APD below breakdown for a lower current level than the circuit limit. After that the circuit sets the bias of the APD above breakdown again waiting for the next avalanche event.

The Geiger-mode operation of a fabricated 16-μm-diameter GaN visible-blind UV *p-i-n* APD (wafer ID: 2-1283-1 with reduced BCB layer on the optical window) was measured in Prof. Joe C. Campbell's group at the University of Virginia. A gated quenching circuit was used and

the schematic is shown in Figure 3.8. Details system setup can be found in [21]. Two most important figures of merit for single photon detection are single photon detection efficiency (SPDE) and dark count probability (DCP). SPDE is the probability of detection of a single incident photon. As defined in Equation 3.2, SPDE is the product of external quantum efficiency (EQE) and the probability of a detectable avalanche event initiated by a generated carrier (avalanche probability). DCP is defined in Equation 3.3 which is the probability per gate of a false positive or error detection due to thermally excited carriers.

$$\text{SPDE} = \eta_{ex} P_a = -\ln\left(\frac{1 - N_{light} / f_{rep}}{1 - N_{dark} / f_{rep}}\right) / \nu \tag{3.2}$$

$$\text{DCP} = N_{dark} / f_{rep} \tag{3.3}$$

Both SPDE and DCP are strongly related to the excess voltage. In Equation 3.2 and 3.3, N_{light} and N_{dark} are the number of counts per second with and without UV illumination, f_{rep} is the laser repetition rate, η_{ex} is EQE at the laser wavelength, P_a is the avalanche probability, and ν is the average number of photons per pulse. Figure 3.9 (a) shows the SPDE and DCP as functions of DC bias. The effective AC pulse width is 1 nanosecond with an amplitude of 12 V. The light source is a pulsed 265 nm UV laser (4.8 photons per pulse) with a repetition frequency of 7.2 KHz. Both the SPDE and DCP increase with the DC bias. The peak SPDE is 1.0 % with DCP of 0.03 under an overall bias of 103.3 V. This is the first front-side-illuminated III-nitride Geiger-mode deep UV APD demonstrated on GaN substrates. The external quantum efficiency of the device at 265 nm is 22%, which is about twice that of PMTs' at this wavelength. A SPDE of 1.0% with an external quantum efficiency of 22% indicates a 4.5% detection rate for the absorbed incident photons.

Another important characteristic of single photon APDs is after-pulsing. After-pulsing is the dark counts induced by the emission of carriers that were trapped in deep levels in the multiplication region during a previous avalanche event. If after-pulsing exist, the DCP will increase with the AC pulse repetition frequency [21]. Figure 3.9 (b) shows dark counts (N_{dark}) versus AC pulse repetition frequency in time duration of 100 seconds. In Figure 3.9 (b) DCP is proportional to the slopes of dark counts curves (from Equation 3.3). Up to 100 KHz dark counts increases linearly with AC pulse frequency, showing that DCP keeps the same as the repetition rate increases. Therefore, there is no after-pulsing effect observed in this GaN UV *p-i-n* Geiger-mode APD up to 100 KHz.

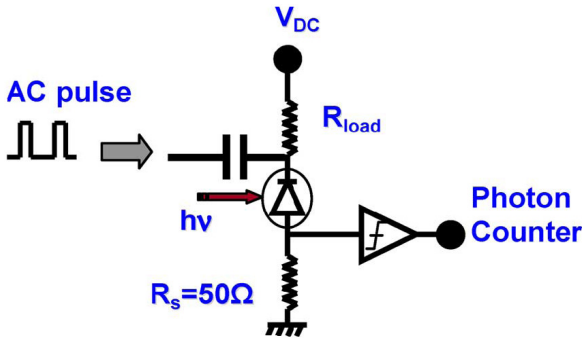

Figure 3.8. The schematic of the measurement circuit for the Geiger-mode operation [21].

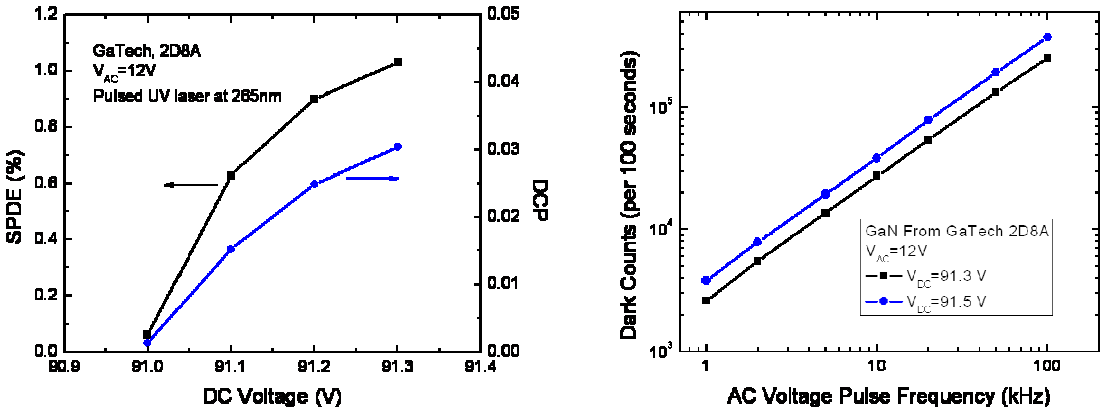

(a) (b)

Figure 3.9. (a) Pulse frequency versus dark counts for a fabricated 16-µm-diameter GaN visible-blind UV *p-i-n* APD in a time duration of 100 seconds (b) SPDE and DCP of the same APD.

3.2 Performance evaluation of low-noise GaN UV *p-i-n* photodiodes

GaN visible-blind UV *p-i-n* APDs can work not only in the Geiger-mode for single photon detection but also in the photovoltaic mode or photoconductive mode as ultra-low noise photodiodes with high responsivity. Responsivity performance has been presented and discussed in Section 3.1.1. In this section, the device reverse-biased and forward-biased I-V characteristics will be presented, showing high-quality GaN visible-blind UV photodiodes with record dark current and record effective detectivity in the low-reverse-biased region. The devices are tested using the same system described in Section 3.1.

3.2.1 I-V characteristics

The reverse-biased I-V curves of a fabricated 80-μm-diameter APD (wafer ID: 2-1283-6) with and without UV illumination are shown in Figure 3.10. The dark current keeps decreasing when biased from 0 V to – 20 V until reaching the system noise floor. It is different with single-mesa photodiodes whose dark current increases with the reverse bias, and can be explained as follows using the double-mesa structure.

The dark current includes generation-recombination (g-r) components arising from the bulk and the surface defects in mesa-etched *p*-*i*-*n* photodiodes, in addition to the diffusion components in the quasi-neutral region. In the low reverse biasing region, the bulk leakage may be insignificant when compared to the surface leakage. A double-mesa ledge structure was proposed to suppress the surface leakage current [64]. During device fabrication, we intentionally leave a 30-nm *p*-layer GaN on top of the second mesa edge to form a ledged structure as discussed in Section 2.4. In the ledged structure, at zero bias, the sidewall surface states are connected to the *p*-type contact through the un-depleted *p*-layer GaN ledge. As the reverse bias increases, the depletion width of the ledged *p*-layer is widened and the resistance between the side-wall surface states and the *p*-type metal contact increases. As a result, the dark current is reduced. When the ledged *p*-layer is fully depleted (at V ~ – 20 V), the surface leakage path will be effectively isolated from the paths of conduction and the overall dark current reaches its minimum.

For reverse biases greater than 30 V (equivalent the electric field > 1 MV/cm), however, the generation current from the bulk space-charge region becomes significant and leads to a monotonic increase before the impact ionization process takes precedence for |V| > 70 V.

Through the sidewall leakage suppression, the measured dark current of < 2 fA (or an equivalent current density of 40 pA/cm2) is achieved for V = – 10 V to – 30 V. To our best knowledge, it is the lowest dark current density reported to date for GaN photodiodes in such biases. The data also show that the photodiode can clearly resolve an input optical power as low as 100 fW at λ = 360 nm.

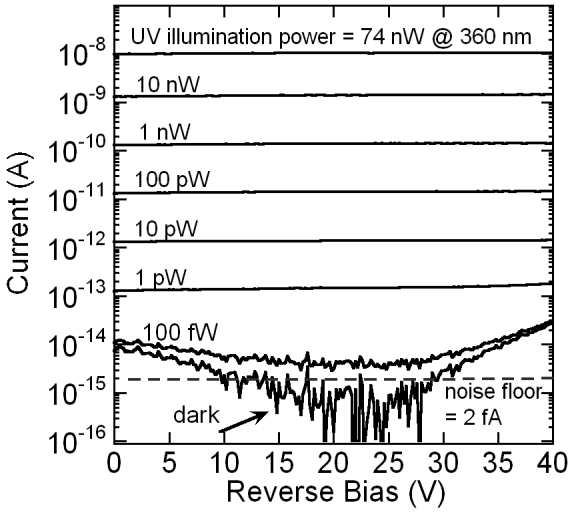

Figure 3.10. Reverse-biased I-V characteristics of a fabricated 80-μm-diameter GaN *p-i-n* photodiode with and without UV light illumination at λ = 360 nm.

Figure 3.11 (a) shows the forward-biased I-V characteristics of fabricated GaN *p-i-n* APDs (wafer ID: 2-1283-6), plotted using the current densities normalized with the mesa areas. Eight devices with four different mesa diameters were taken randomly from a 1 cm^2 wafer piece. It is observed that these devices show very low current density (< 2 nA/cm^2) in the general-recombination current region, indicating high epitaxial quality and effective suppression of leakage paths in the fabricated diodes through the double-mesa surface depletion method. In the diffusion-current region, the ideality factor has a mean value of 2.01 with a standard deviation of 0.01, indicating that the space-charge recombination dominates the carrier transport. The

increased current density deviation in the series-resistance region is possibly due to the non-uniform current distribution as the device diameter increases.

In Figure 3.11 (b), to further study the efficacy of using the two-mesa surface depletion technique [64] and the source of the leakage current from the photodiode mesa, forward-biased current densities from those eight devices at fixed bias of 2.5V are plotted as a function of the inverse of device radius [63]. In forward-biased diffusion-current region, device current can be expressed as Equation 3.4, where background noise is not included since it is at least six orders of magnitude smaller. Equation 3.5 is derived form Equation 3.4 by dividing the device mesa area on both sides of this equation. As shown in Figure 3.11 (b), the trend of curve fitting for these current density values is flat versus the inverse of device radius, indicating that surface traps are not a contributing factor in the fabricated GaN *p-i-n* diodes with the double-mesa *p-n* junction surface depletion technique.

$$I = J_{bulk} \times area + J_{sidewall} \times perimeter \tag{3.4}$$

$$I = J_{bulk} + J_{sidewall} \times 2 / radius \tag{3.5}$$

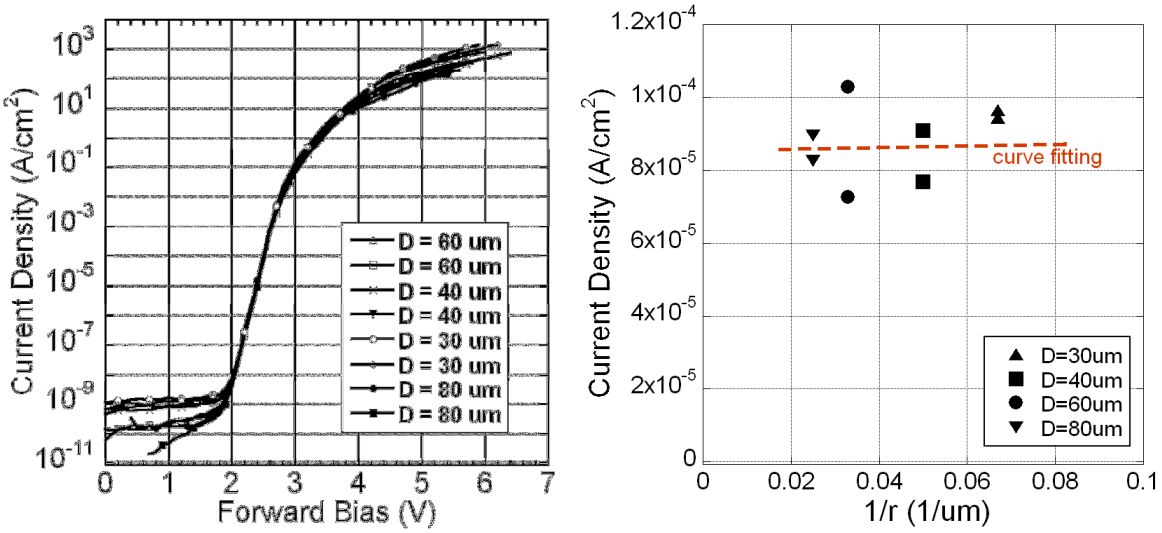

(a) (b)

Figure 3.11. (a) Forward-biased I-V characteristics of the fabricated GaN APDs with different mesa areas (b) A plot of current density versus the inverse of the device radii at bias of 2.5 V.

3.2.2 Thermally-limited device noise performance in the photovoltaic mode

To evaluate the noise performance in a *p-i-n* photodiode, two important figures of merit are noise equivalent power (NEP) and detectivity (D*). NEP is defined as the incident root mean square optical power required to produce a signal-to-noise ratio of one in a 1-Hz bandwidth [4]. The major noise sources for a photodiode are shot noise and thermal noise. Shot noise is caused by the current from optical illumination, background radiation, and thermally-generated electron-hole pairs. For wide-bandgap UV visible-blind or solar-blind photodiodes operating in the photovoltaic mode, it is reasonable to ignore the effects of background radiation and thermal-generated electro-hole pairs. Only the thermal noise as the primary noise source is considered in the zero-biased device NEP calculation (set optical illumination = 0), which is called the thermally-limited condition [43, 44, 99]. The thermally-limited NEP is given by Equation 3.6 [4], where R_λ is the responsivity at the selected optical wavelength (137 mA/W @ λ = 360 nm and 0

V) and R_o is the differential resistance of the photodiode at 0 V. The corresponding detectivity D* is given by Equation 3.7, where A is the optical detection area.

$$NEP = \frac{\sqrt{4kT / R_0}}{R_\lambda} \quad \text{W·Hz}^{-0.5} \tag{3.6}$$

$$D^* = \frac{\sqrt{A}}{NEP} \quad \text{cm·Hz}^{0.5}\text{·W}^{-1} \tag{3.7}$$

The differential resistance R_o is extracted by the curve fitting of the reverse-biased and forward-biased dark current data near 0 V. In Figure 3.12 exponential curve fitting is performed for the 80-µm-diameter device (the same device in Figure 3.10) using data from - 10 V to - 0 V and from + 0 V to 1 V. The fitted I-V relationship is shown in Equation 3.8 and is also plotted in Figure 3.12 with the measurement data points.

$$I = -9.69\times10^{-15} e^{0.132V} + 9.07\times10^{-15} e^{0.383V} . \tag{3.8}$$

$$R_0 \mid_{V=0} = (\partial I / \partial V)^{-1} \mid_{V=0} = 1/(-9.69\times10^{-15}\times0.132 + 9.07\times10^{-15}\times0.383) = 4.56\times10^{14}\,\Omega . \tag{3.9}$$

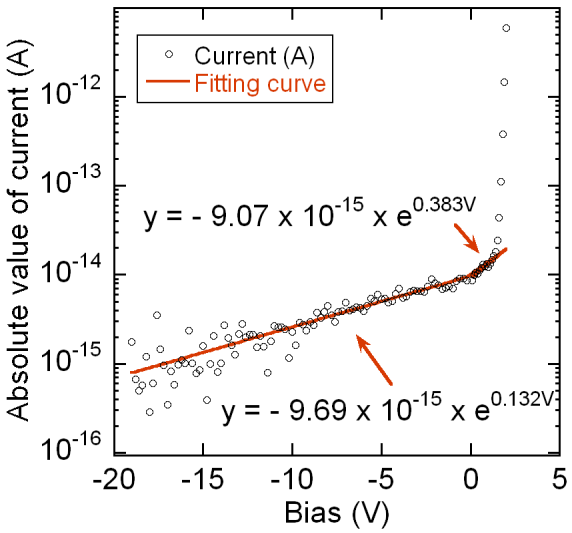

Figure 3.12. Curve-fitting of the reverse-biased and forward-biased dark current data near 0 V for an 80-µm-diamter GaN *p-i-n* photodiode in the photovoltaic mode.

The differential resistance R_o is obtained from Equation 3.8 by $(\partial I/\partial V)^{-1}$ as shown in Equation 3.9. At zero-bias the R_o is 4.56×10^{14} Ω. From Equation 3.6, at λ = 360 nm the room-temperature (T = 293 K) thermal-limited NEP is 4.35×10^{-17} W·Hz$^{-0.5}$ at 0 V, which corresponds to a detectivity D^* = A$^{0.5}$/NEP = 1.63×10^{14} cm·Hz$^{0.5}$·W^{-1}. The NEP and D* values are among the best values reported for GaN visible-blind UV *p-i-n* photodiodes to date.

3.2.3 Device noise performance in the photoconductive mode

Most of the reported III-nitride UV *p-i-n* photodiodes were evaluated in the photovoltaic mode (zero biasing) with the thermally-limited assumption for the maximum detectivity. On the other hand, the photoconductive mode (reverse biasing) can provide the benefits of higher linearity, increased response speed as well as higher responsivity, which are very important for many practical applications.

As observed in Section 3.2.1, the "sweet spots" for low-noise photodiodes could be achieved around V = – 20 V, where the dark current reaches its minimum. For such biases, the photoconductive detection mode can be realized. In this section, the device noise performance of the GaN UV photodiodes in the photoconductive mode is presented. In this mode, the thermal-limited assumption cannot be made because the generation-current-induced shot noise cannot be ignored. The resulting NEP and D* should be evaluated by Equation 3.10 and Equation 3.7 , respectively, where I_d is the dark current, R_λ is the responsivity at the selected wavelength, R_V is the device differential resistance, and A is the mesa area [4].

$$NEP = \frac{\sqrt{2qI_d + 4kT/R_V}}{R_\lambda} \quad \text{W·Hz}^{-0.5} \tag{3.10}$$

R_V and I_d are extracted by curve fitting of the dark current using the measured data from – 25 V to – 35 V for a meaningful data extrapolation. The fitted I-V relationship is shown in Equation 3.11. The differential resistance is then obtained by $(\partial I/\partial V)^{-1}$ as shown in Equation 3.12. At – 20 V, the R_V is 3.03×10^{16} Ω and the fitted I_d is 1.10×10^{-16} A as shown in Equation 3.13. The corresponding room-temperature (293K) NEP is 4.27×10^{-17} W-Hz$^{-0.5}$ and the D^* is 1.66×10^{14} cm-Hz$^{0.5}$-W^{-1} at λ = 360 nm. The NEP and D* values are the best values reported for GaN visible-blind UV *p-i-n* photodiodes operating at reverse bias to date. It is noticed that in the photoconductive mode the NEP is limited by the I_d-induced shot noise and the thermal noise is only about 1% of the overall noise at – 20 V.

$$I = 2.73\times10^{-19} e^{0.300V} . \tag{3.11}$$

$$R_0 \mid_{V=20} = (\partial I/\partial V)^{-1} \mid_{V=20} = 1/(2.73\times10^{-19} \times 0.300 \times \exp(0.300\times 20)) = 3.03\times10^{16}\,\Omega \tag{3.12}$$

$$I(V = 20) = 2.73\times10^{-19} e^{0.300*20} = 1.10\times10^{-16}(A) \tag{3.13}$$

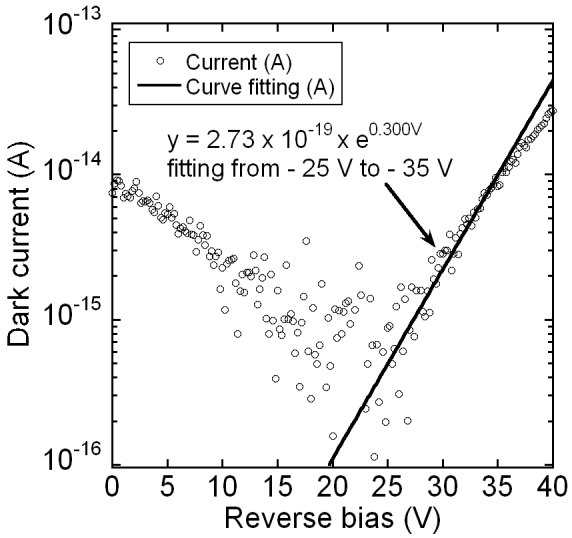

Figure 3.13. Curve-fitting of the reverse-biased dark current data near from – 25 V to – 35 V for an 80-μm-diamter GaN *p-i-n* photodiode.

CHAPTER 4 CONCLUSIONS

We have fabricated and characterized high-performance GaN homojunction UV *p-i-n* APDs. Significant device leakage current suppression is achieved through the use of optimized sidewall leakage reduction methods as well as the free-standing bulk GaN substrates.

A GaN APD device with the size of 570 um^2 shows a linear-mode avalanche gain > 10^5 at λ = 360 nm, which is the highest avalanche gain for III-nitride APDs reported to date. At the deep UV wavelength of 280 nm, a gain greater than 10^4 is also achieved. The Geiger-mode operation is demonstrated on a 16-μm-diamter device. The single photon detection efficiency (SPDE) is 1.0 % at 265 nm with dark count probability (DCP) of 0.03. This is the first Geiger-mode deep UV APDs reported using a front-illuminated homojunction *p-i-n* diode structure on a free-standing bulk GaN substrate.

The APDs can also work as low-noise, high-sensitivity UV photodiodes in both the photoconductive mode and photovoltaic mode. For an 80-μm-diameter photodiode, the dark current density is as low as 40 pA/cm^2 at – 20 V and its responsivity is 0.140 A/W at 360 nm. The minimum detectable optical power can be as low as 100 fW at λ = 360 nm. The room-temperature NEP of 4.27×10^{-17} W-$Hz^{-0.5}$ and D^* of 1.66×10^{14} cm-$Hz^{0.5}$-W^{-1} are also obtained at – 20 V for the photoconductive mode.

The future work is to improve the SPDE in the Geiger-mode operation. The focus will be on the dark current reduction in the avalanche region. To achieve this purpose, the *p-i-n* APD

structure may be optimized to suppress the field-assisted tunneling at breakdown, and SAM APDs may be also developed for lower multiplication noise and higher avalanche gains.

REFERENCES

[1] http://kottan-labs.bgsu.edu/teaching/workshop2001/chapter5_files/image018.jpg. April 30, 2009

[2] http://www.ioffe.rssi.ru/SVA/NSM/Semicond/GaN/index.html. April 30, 2009

[3] http://www.ioffe.rssi.ru/SVA/NSM/Semicond/SiC/index.html. April 30, 2009

[4] S. M. Sze and K. K. Ng, *Physics of Semiconductor Devices*, third ed. New York: Wiley, 2007.

[5] http://www.semiconductors.co.uk/nitrides.htm. April 30, 2009

[6] http://www.ioffe.rssi.ru/SVA/NSM/Semicond/InP/index.html. April 30, 2009

[7] http://www.ioffe.rssi.ru/SVA/NSM/Semicond/Ge/index.html. April 30, 2009

[8] http://www.ioffe.rssi.ru/SVA/NSM/Semicond/AlN/index.html. April 30, 2009

[9] http://www.ioffe.rssi.ru/SVA/NSM/Semicond/InN/index.html. April 30, 2009

[10] http://www.ecse.rpi.edu/~schubert/Light-Emitting-Diodes-dot-org/chap12/chap12.htm. April 30, 2009

[11] http://en.wikipedia.org/wiki/Ultraviolet#Natural_sources_of_UV. April 30, 2009

[12] G. A. Wilson and J. Brady, "Design considerations and signal processing algorithms for laser-induced fluorescence airborne pathogen sensors," in *Optically Based Biological and Chemical Sensing for Defence*, London, United Kingdom, 2004, pp. 1-13.

[13] M. Razeghi and A. Rogalski, "Semiconductor ultraviolet detectors," in *Photodetectors: Materials and Devices*, San Jose, CA, USA, 1996, pp. 114-125.

[14] C. Pernot, A. Hirano, M. Iwaya, T. Detchprohm, H. Amano, I. Akasaki, "Demonstration of Flame Detection in Room Light Background by Solar-Blind AlGaN PIN Photodiode," *physica status solidi (a),* vol. 188, pp. 293-296, 2001.

[15] G. A. Shaw, A. M. Siegel, J. Model, and D. Greisokh, "Recent progress in short-range ultraviolet communication," in *Unattended Ground Sensor Technologies and Applications VII*, Orlando, FL, USA, 2005, pp. 214-225.

[16] http://sales.hamamatsu.com/en/products/electron-tube-division/detectors/photomultiplier-tubes.php. April 30, 2009

[17] http://sales.hamamatsu.com/en/products/solid-state-division/si-photodiode-series/si-apd.php. April 30, 2009

[18] A. O. Konstantinov, Q. Wahab, N. Nordell, and U. Lindefelt, "Ionization rates and critical fields in 4H silicon carbide," *Applied Physics Letters,* vol. 71, pp. 90-92, 1997.

[19] L. Han-Din, G. Xiangyi, D. McIntosh, and J. C. Campbell, "Demonstration of ultraviolet 6H-SiC PIN avalanche photodiodes," *IEEE Photonics Technology Letters,* vol. 18, pp. 2508-10, 2006.

[20] B. Xiaogang, G. Xiangyi, D. C. McIntosh, L. Han-Din, and J. C. Campbell, "High detection sensitivity of ultraviolet 4H-SiC avalanche photodiodes," *IEEE Journal of Quantum Electronics,* vol. 43, pp. 1159-62, 2007.

[21] B. Xiaogang, D. McIntosh, L. Handin, and J. C. Campbell, "Ultraviolet single photon detection with Geiger-mode 4H-SiC avalanche photodiodes," *IEEE Photonics Technology Letters,* vol. 19, pp. 1822-4, 2007.

[22] B. Butun, T. Tut, E. Ulker, T. Yelboga, and E. Ozbay, "High-performance visible-blind GaN-based p-i-n photodetectors," *Applied Physics Letters,* vol. 92, pp. 033507-1, 2008.

[23] C. L. Yu, C. H. Chen, S. J. Chang, and P. C. Chang, "GaN metal-semiconductor-metal ultraviolet photodetectors with Ir/Pt contact electrodes," *Journal of the Electrochemical Society,* vol. 154, pp. 71-2, 2007.

[24] T. Tut, M. Gokkavas, A. Inal, and E. Ozbay, "AlxGa1-xN-based avalanche photodiodes with high reproducible avalanche gain," *Applied Physics Letters,* vol. 90, pp. 163506-1, 2007.

[25] G. Xiangyi, L. B. Rowland, G. T. Dunne, J. A. Fronheiser, P. M. Sandvik, A. L. Beck, and J. C. Campbell, "Demonstration of ultraviolet separate absorption and multiplication 4H-SiC avalanche photodiodes," *IEEE Photonics Technology Letters,* vol. 18, pp. 136-8, 2006.

[26] J. B. Limb, D. Yoo, J. H. Ryou, W. Lee, S. C. Shen, R. D. Dupuis, M. L. Reed, C. J. Collins, M. Wraback, D. Hanser, E. Preble, N. M. Williams, and K. Evans, "GaN ultraviolet avalanche photodiodes with optical gain greater than 1000 grown on GaN substrates by metal-organic chemical vapor deposition," *Applied Physics Letters,* vol. 89, pp. 11112-1, 2006.

[27] M. C. Chen, J. K. Sheu, M. L. Lee, C. J. Tun, and G. C. Chi, "Improved performance of planar GaN-based p-i-n photodetectors with Mg-implanted isolation ring," *Applied Physics Letters,* vol. 89, pp. 183509-1, 2006.

[28] J. L. Pau, R. McClintock, K. Minder, C. Bayram, P. Kung, M. Razeghi, Mu, ntilde, E. oz, and D. Silversmith, "Geiger-mode operation of back-illuminated GaN avalanche photodiodes," *Applied Physics Letters,* vol. 91, pp. 041104-1, 2007.

[29] K. Minder, J. L. Pau, R. McClintock, P. Kung, C. Bayram, M. Razeghi, and D. Silversmith, "Scaling in back-illuminated GaN avalanche photodiodes," *Applied Physics Letters,* vol. 91, pp. 073513-1, 2007.

[30] S.-C. Shen, Y. Zhang, D. Yoo, J.-B. Limb, J.-H. Ryou, P. D. Yoder, and R. D. Dupuis, "Performance of deep ultraviolet GaN avalanche photodiodes grown by MOCVD," *IEEE Photonics Technology Letters,* vol. 19, pp. 1744-6, 2007.

[31] D. Yoo, J. Limb, J.-H. Ryou, Y. Zhang, S.-C. Shen, R. D. Dupuis, D. Hanser, E. Preble, and K. Evans, "AlxGa1-xN ultraviolet avalanche photodiodes grown on GaN substrates," *IEEE Photonics Technology Letters,* vol. 19, pp. 1313-15, 2007.

[32] Y. Zhang, D. Yoo, J.-B. Limb, J.-H. Ryou, R. D. Dupuis, and S.-C. Shen, "GaN ultraviolet avalanche photodiodes fabricated on free-standing bulk GaN substrates," *physica status solidi (c),* vol. 5, pp. 2290-2292, 2008.

[33] C. Bayram, J. L. Pau, R. McClintock, and M. Razeghi, "Performance enhancement of GaN ultraviolet avalanche photodiodes with p-type δ-doping," *Applied Physics Letters,* vol. 92, pp. 241103-1, 2008.

[34] C. Bayram, J. L. Pau, R. McClintock, M. Razeghi, M. P. Ulmer, and D. Silversmith, "High quantum efficiency back-illuminated GaN avalanche photodiodes," *Applied Physics Letters,* vol. 93, p. 211107 (3 pp.), 2008.

[35] J. L. Pau, C. Bayram, R. McClintock, M. Razeghi, and D. Silversmith, "Back-illuminated separate absorption and multiplication GaN avalanche photodiodes," *Applied Physics Letters,* vol. 92, pp. 101120-1, 2008.

[36] W. B. Liu, D. G. Zhao, X. Sun, S. Zhang, D. S. Jiang, H. Wang, S. M. Zhang, Z. S. Liu, J. J. Zhu, Y. T. Wang, L. H. Duan, and H. Yang, "Stable multiplication gain in GaN p-i-n avalanche photodiodes with large device area," *Journal of Physics D: Applied Physics,* vol. 42, p. 015108 (5 pp.), 2009.

[37] R. D. Dupuis, R. Jae-Hyun, S. Shyh-Chiang, P. D. Yoder, Z. Yun, K. Hee Jin, C. Suk, and Z. Lochner, "Growth and fabrication of high-performance GaN-based ultraviolet avalanche photodiodes," *Journal of Crystal Growth,* vol. 310, pp. 5217-22, 2008.

[38] K. H. Lee, P. C. Chang, S. J. Chang, C. L. Yu, Y. C. Wang, and S. L. Wu, "GaN MSM photodetectors with an unactivated Mg-doped GaN cap layer and sputtered ITO electrodes," *Journal of the Electrochemical Society,* vol. 155, pp. 165-167, 2008.

[39] K. T. Lam, P. C. Chang, S. J. Chang, C. L. Yu, Y. C. Lin, Y. X. Sun, and C. H. Chen, "Nitride-based photodetectors with unactivated Mg-doped GaN cap layer," *Sensors & Actuators: A. Physical,* vol. 143, pp. 191-5, 2008.

[40] Z. Yi, C. Ahyi, C. C. Tin, J. Williams, P. Minseo, K. Dong-Joo, C. An-Jen, W. Dake, A. Hanser, E. A. Preble, N. M. Williams, and K. Evans, "Fabrication and device characteristics of Schottky-type bulk GaN-based "visible-blind" ultraviolet photodetectors," *Applied Physics Letters,* vol. 90, pp. 121118-1, 2007.

[41] S. Senda, H. Jiang, and T. Egawa, "AlInN-based ultraviolet photodiode grown by metal organic chemical vapor deposition," *Applied Physics Letters,* vol. 92, pp. 203507-1, 2008.

[42] M. L. Lee, C. Ping-Feng, and J. K. Sheu, "Photodetectors formed by an indium tin oxide/zinc oxide/p-type gallium nitride heterojunction with high ultraviolet-to-visible rejection ratio," *Applied Physics Letters,* vol. 94, p. 013512 (3 pp.), 2009.

[43] N. Biyikli, I. Kimukin, O. Aytur, and E. Ozbay, "Solar-blind AlGaN-based p-i-n photodiodes with low dark current and high detectivity," *IEEE Photonics Technology Letters,* vol. 16, pp. 1718-20, 2004.

[44] C. J. Collins, T. Li, D. J. H. Lambert, M. M. Wong, R. D. Dupuis, and J. C. Campbell, "Selective regrowth of $Al_{0.30}Ga_{0.70}N$ p-i-n photodiodes," *Applied Physics Letters,* vol. 77, pp. 2810-2812, 2000.

[45] J. B. Limb, D. Yoo, Y. Zhang, J. H. Ryou, S. C. Shen, and R. D. Dupuis, "GaN ultraviolet avalanche photodiodes grown on 6H-SiC substrates with SiN passivation," *Electronics Letters,* vol. 44, pp. 313-15, 2008.

[46] S. Verghese, K. A. McIntosh, R. J. Molnar, L. J. Mahoney, R. L. Aggarwal, M. W. Geis, K. M. Molvar, E. K. Duerr, and I. Melngailis, "GaN avalanche photodiodes operating in linear-gain mode and Geiger mode," *IEEE Transactions on Electron Devices,* vol. 48, pp. 502-11, 2001.

[47] R. McClintock, J. L. Pau, K. Minder, C. Bayram, P. Kung, and M. Razeghi, "Hole-initiated multiplication in back-illuminated GaN avalanche photodiodes," *Applied Physics Letters,* vol. 90, pp. 141112-1, 2007.

[48] Y. Z. Chiou, "Leakage current analysis of nitride-based photodetectors by emission microscopy inspection," *IEEE Sensors Journal,* vol. 8, pp. 1506-10, 2008.

[49] J. P. Liu, J. H. Ryou, D. Yoo, Y. Zhang, J. Limb, C. A. Horne, S. C. Shen, R. D. Dupuis, A. D. Hanser, E. A. Preble, and K. R. Evans, "III-nitride heterostructure field-effect transistors grown on semi-insulating GaN substrate without regrowth interface charge," *Applied Physics Letters,* vol. 92, pp. 133513-1, 2008.

[50] J. Liu, J.-H. Ryou, Z. Lochner, J. Limb, D. Yoo, R. D. Dupuis, Z. Wu, A. M. Fischer, and F. A. Ponce, "Surface morphology control of green LEDs with p-InGaN layers grown by metalorganic chemical vapor deposition," *Journal of Crystal Growth,* vol. In Press, Corrected Proof, 2008.

[51] I. Adesida, C. Youtsey, A. T. Ping, F. Khan, L. T. Romano, and a. G. Bulman, "Dry and wet etching for group III-nitrides," Boston, MA, USA, 1999, pp. 1-4.

[52] Y. Bo and P. Fay, "Etch rate and surface morphology control in photoelectrochemical etching of GaN," *Journal of Vacuum Science & Technology B (Microelectronics and Nanometer Structures),* vol. 22, pp. 1750-4, 2004.

[53] P. Lung-Han, C. W. Chuang, Y. C. Hsu, J. K. Ho, C. N. Huang, and C. Y. Chen, "Hydration effects in the photoassisted wet chemical etching of gallium nitride," *IEEE Journal of Selected Topics in Quantum Electronics,* vol. 4, pp. 564-9, 1998.

[54] B. S. Shelton, T. G. Zhu, M. M. Wong, H. K. Kwon, C. J. Eiting, D. J. H. Lambert, S. P. Turini, and R. D. Dupuis, "Ultrasmooth GaN etched surfaces using photoelectrochemical wet etching and an ultrasonic treatment," *Electrochemical and Solid-State Letters,* vol. 3, pp. 87-9, 2000.

[55] J. Skriniarova, P. Bochem, A. Fox, and P. Kordos, "Photoenhanced wet etching of gallium nitride in KOH-based solutions," *Journal of Vacuum Science & Technology B (Microelectronics and Nanometer Structures),* vol. 19, pp. 1721-7, 2001.

[56] C. Youtsey, I. Adesida, and G. Bulman, "Broad-area photoelectrochemical etching of GaN," *Electronics Letters,* vol. 33, pp. 245-6, 1997.

[57] L. Ma, K. Addeni, C. Zeng, Y. Jin, K. Dandu, Y. Saripalli, M. Johnson, and D. Barlage, "Comparison of different GaN Etching Techniques," in *2006 CS MANTECH* Vancouver, BC, Canada,, 2006.

[58] J. A. Bardwell, J. B. Webb, H. Tang, J. Fraser, and S. Moisa, "Ultraviolet photoenhanced wet etching of GaN in K2S2O8 solution," *Journal of Applied Physics,* vol. 89, pp. 4142-9, 2001.

[59] Z. H. Hwang, J. M. Hwang, H. L. Hwang, and W. H. Hung, "Electrodeless wet etching of GaN assisted with chopped ultraviolet light," *Applied Physics Letters,* vol. 84, pp. 3759-61, 2004.

[60] C. Youtsey, L. T. Romano, R. J. Molnar, and I. Adesida, "Rapid evaluation of dislocation densities in n-type GaN films using photoenhanced wet etching," *Applied Physics Letters,* vol. 74, pp. 3537-3539, 1999.

[61] Y. Zhang, J.-H. Ryou, R. D. Dupuis, and S.-C. Shen, "A Surface Treatment Technique for III-N Device Fabrication," in *2008 CS MANTECH* Chicago, Illinois, USA, 2008.

[62] Z. Tinggang, "Development of Photoelectrochemical Etching for III-Nitride Devices Grown by Metalorganic Chemical Vapor Deposition." vol. Master of Science in Engineering Austin: The University of Texas at Austin, 2000.

[63] W. Liu, *Fundamentals of III-V Devices: HBTs, MESFETs, and HFETs/HEMTs*, 1 ed., 1999.

[64] Y. Zhang, B. Narayan, and S.-C. Shen, "Sidewall Leakage Reduction in Mesa-Etched PN Junctions Using a Surface Depletion Technique," in *IWN 2008* Montreux, Switzerland, 2008.

[65] P. Bhattacharya, *Semiconductor Optoelectronic Devices*, second ed. New Jersey: Prentice Hall, 1997.

[66] J. K. Sheu, Y. K. Su, G. C. Chi, M. J. Jou, C. M. Chang, C. C. Liu, and W. C. Hung, "High-transparency Ni/Au Ohmic contact to p-type GaN," Tokyo, Japan, 1998, pp. 638-41.

[67] L.-C. Chen, J.-K. Ho, F.-R. Chen, J.-J. Kai, L. Chang, C.-S. Jong, C. C. Chiu, C.-N. Huang, and K.-K. Shih, "The effect of heat treatment on Ni/Au ohmic contacts to p-type GaN," Germany, 1999, pp. 773-7.

[68] C. Li-Chien, C. Fu-Rong, K. Ji-Jung, C. Li, H. Jin-Kuo, J. Charng-Shyang, C. C. Chiu, H. Chao-Nien, C. Chin-Yuen, and S. Kwang-Kuo, "Microstructural investigation of oxidized Ni/Au ohmic contact to p-type GaN," *Journal of Applied Physics,* vol. 86, pp. 3826-32, 1999.

[69] J. Ja-Soon, P. Seong-Ju, and S. Tae-Yeon, "Ultrahigh transparency of Ni/Au ohmic contacts to surface-treated p-type GaN," *Journal of Applied Physics,* vol. 88, pp. 5490-2, 2000.

[70] L. Jong-Lam, K. Jong Kyu, L. Jae Won, P. Yong Jo, and K. Taeil, "Transparent Pt ohmic contact on p-type GaN with low resistivity using $(NH_4)_2S_x$ treatment," *Electrochemical and Solid-State Letters,* vol. 3, pp. 53-5, 2000.

[71] D. Qiao, L. S. Yu, S. S. Lau, J. Y. Lin, H. X. Jiang, and T. E. Haynes, "A study of the Au/Ni ohmic contact on p-GaN," *Journal of Applied Physics,* vol. 88, pp. 4196-200, 2000.

[72] C. H. Lin, D. L. Hibbard, A. Au, H. P. Lee, Z. J. Dong, F. J. Szalkowski, J. Chen, and C. Chen, "Low resistance optically transparent contacts to p-type GaN using oxidized Ni/Au and ITO for LED application," Warrendale, PA, USA, 2001, pp. 4-8.

[73] Y. S. Chang, T. S. Huang, and C. Y. Nee, "Electrical and optical characteristics of Au/Ni ohmic contacts to p-GaN," Hong Kong, China, 2003, p. 107.

[74] Z. Z. Chen, Z. X. Qin, Y. Z. Tong, X. D. Hu, T. J. Yu, Z. J. Yang, X. M. Ding, Z. H. Li, and G. Y. Zhang, "Thermal annealing effects on Ni/Au contacts to p type GaN in different ambient," *Materials Science & Engineering B (Solid-State Materials for Advanced Technology),* vol. B100, pp. 199-203, 2003.

[75] J. Ho Won and L. Jong-Lam, "Mechanism for ohmic contact formation of Ni/Ag contacts on p-type GaN," *Applied Physics Letters,* vol. 85, pp. 5920-2, 2004.

[76] O. S. June, L. Dong-Seok, K. Sang-Ho, J. S. Kwak, O. H. Nam, Y. Park, and S. Tae-Yeon, "GaN-based light-emitting diodes with Ni-Mg solid solution/Au p-type ohmic contact," *Solid-State Electronics,* vol. 48, pp. 1597-600, 2004.

[77] H. Yang, Z.-x. Qin, Z.-z. Chen, C.-y. Hu, X.-d. Hu, T.-j. Yu, Z.-j. Yang, and G.-y. Zhang, "Characteristics of Ni/Au contact to p-GaN annealed in air and oxygen ambient," *Chinese Journal of Luminescence,* vol. 25, pp. 691-5, 2004.

[78] J. W. Bae, T. Hossain, I. Adesida, K. H. Bogart, D. Koleske, A. A. Allerman, and J. H. Jang, "Low resistance ohmic contact to p-type GaN using Pd/Ir/Au multilayer scheme," *Journal of Vacuum Science & Technology B (Microelectronics and Nanometer Structures),* vol. 23, pp. 1072-5, 2005.

[79] H. K. Cho, T. Hossain, J. W. Bae, and I. Adesida, "Characterization of Pd/Ni/Au ohmic contacts on p-GaN," *Solid-State Electronics,* vol. 49, pp. 774-8, 2005.
[80] J. L. Yang, J. S. Chen, and S. J. Chang, "Presence of nanosize Au dots on the formation of ohmic contact for the Ni-Au base film to p-GaN," *Journal of Vacuum Science & Technology B (Microelectronics and Nanometer Structures),* vol. 23, pp. 2127-31, 2005.
[81] C. Y. Hu, Z. X. Qin, Z. X. Feng, Z. Z. Chen, Z. B. Ding, Z. J. Yang, T. J. Yu, X. D. Hu, S. D. Yao, and G. Y. Zhang, "Temperature dependent diffusion and epitaxial behavior of oxidized Au/Ni/p-GaN ohmic contact," *Materials Science & Engineering B (Solid-State Materials for Advanced Technology),* vol. 128, pp. 37-43, 2006.
[82] D. L. Hibbard, S. P. Jung, C. Wang, D. Ullery, Y. S. Zhao, H. P. Lee, W. So, and H. Liu, "Low resistance high reflectance contacts to p-GaN using oxidized Ni/Au and Al or Ag," *Applied Physics Letters,* vol. 83, pp. 311-13, 2003.
[83] Z. Hassan, Y. C. Lee, F. K. Yam, Z. J. Yap, N. Zainal, H. B. Hassan, and K. Ibrahim, "Thermal stability of Ni/Ag contacts on p-type GaN," *Physica Status Solidi C,* pp. 2528-32, 2004.
[84] J. Ho Won, K. Jong Kyu, K. Soo Young, Y. Hak Ki, and L. Jong-Lam, "Ohmic contacts for high power LEDs," Gyeongju, South Korea, 2004, pp. 2831-6.
[85] J. Ho Won and L. Jong-Lam, "Low-resistance and high-reflectance Ni/Ag/Ru/Ni/Au ohmic contact on p-type GaN," *Applied Physics Letters,* vol. 85, pp. 4421-3, 2004.
[86] C. W. Lim, C. K. Tan, A. Abdul Aziz, Z. Hassan, and F. K. Yam, "Multi layer metallization scheme (Ni/Pd/Ag) ohmic contact on p-type GaN," Kuala Lumpur, Malaysia, 2004, p. 5 pp.
[87] K. Soo Young and L. Jong-Lam, "Highly reflective and low-resistant Ni/Au/ITO/Ag Ohmic contact on p-type GaN," *Electrochemical and Solid-State Letters,* vol. 7, pp. 102-4, 2004.
[88] L. Dong-Seok, M. Jeong-Tae, L. Dae-Yong, and S. Tae-Yeon, "Formation of high-quality Ohmic contacts to p-GaN for flip-chip LEDs using Ag/TiNx/Al," *Electrochemical and Solid-State Letters,* vol. 8, pp. 150-2, 2005.
[89] J. O. Song, L. Dong-Seok, K. Joon Seop, Y. Park, S. W. Chae, and S. Tae-Yeon, "Improvement of the luminous intensity of light-emitting diodes by using highly transparent Ag-indium tin oxide p-type ohmic contacts," *IEEE Photonics Technology Letters,* vol. 17, pp. 291-3, 2005.
[90] H.-X. Ma, Y.-J. Han, W.-J. Shentu, X.-P. Zhang, and Y. Luo, "A novel Ni/Ag/Pt Ohmic contact to P-type GaN for flip-chip light-emitting diodes," *Chinese Physics Letters,* vol. 23, pp. 2299-302, 2006.
[91] C. H. Chou, C. L. Lin, Y. C. Chuang, H. Y. Bor, and C. Y. Liu, "High thermally stable Ni/Ag(Al) alloy contacts on p-GaN," *Applied Physics Letters,* vol. 90, pp. 22103-1, 2007.
[92] C. Liann-Be, S. Ching-Chuan, and J. Ming-Jer, "The reflectivity enhancement of Ni/Ag/(Ti or Mo)/Au ohmic contact for flip-chip light-emitting diode applications," Catania, Sicily, Italy, 2007, pp. 177-80.
[93] J. Song and S. Tae-Yeon, "Highly transparent Ag/SnO2 ohmic contact to p-type GaN for ultraviolet light-emitting diodes," *Applied Physics Letters,* vol. 85, pp. 6374-6, 2007.

[94] K. Sunjung, J. Jun-Ho, and L. Jeong-Soo, "Thermally stable and highly reflective ITO/Ag-based ohmic contacts to p-GaN," *Journal of the Electrochemical Society,* vol. 154, pp. 973-6, 2007.
[95] D.-S. Zhao, S.-M. Zhang, L.-H. Duan, Y.-T. Wang, D.-S. Jiang, W.-B. Liu, B.-S. Zhang, and H. Yang, "Effects of Ag on electrical properties of Ag/Ni/p-GaN Ohmic contact," *Chinese Physics Letters,* vol. 24, pp. 1741-4, 2007.
[96] J. B. Limb, "DESIGN, FABRICATION AND CHARACTERIZATION OF III-NITRIDE PN JUNCTION DEVICES," in *School of Electrical and Computer Engineering*. vol. Doctor of Philosophy Atlanta: Georgia Institute of Technology, 2007.
[97] W. Lee, J. Limb, J.-H. Ryou, D. Yoo, T. Chung, and R. D. Dupuis, "Effect of thermal annealing induced by p-type layer growth on blue and green LED performance," *Journal of Crystal Growth,* vol. 287, pp. 577-581, 2006.
[98] S. Cova, M. Ghioni, A. Lacaita, C. Samori, and F. Zappa, "Avalanche photodiodes and quenching circuits for single-photon detection," *Appl. Opt.,* vol. 35, pp. 1956-1976, 1996.
[99] M. L. Lee, J. K. Sheu, Y. K. Su, S. J. Chang, W. C. Lai, and G. C. Chi, "Reduction of dark current in AlGaN-GaN Schottky-barrier photodetectors with a low-temperature-grown GaN cap layer," *IEEE Electron Device Letters,* vol. 25, pp. 593-5, 2004.